Palaeogeography, Palaeoclimatology, Palaeoecology 612 (2023) 111376

Contents lists available at ScienceDirect

Palaeogeography, Palaeoclimatology, Palaeoecology

journal homepage: www.elsevier.com/locate/palaeo

Periodic paleo-environment oscillation on multi-timescales in the Triassic and their significant implications for algal blooms: A case study on the lacustrine shales in Ordos Basin

Miruo Lin [a], Kelai Xi [a,*], Yingchang Cao [a], Keyu Liu [a], Rukai Zhu [b]

[a] *Key Laboratory of Deep Oil and Gas, China University of Petroleum (East China), Qingdao 266580, China*
[b] *Research Institute of Petroleum Exploration and Development, PetroChina, Beijing 100083, China*

ARTICLE INFO

Editor: S. Shen

Keywords:
Triassic climate
Astronomical cycle
Solar activity
ENSO-like cycle
Algae bloom

ABSTRACT

The Triassic climate has been a relatively neglected topic and conventionally considered a “hot-house” world. Using detailed petrographic characterization, in situ geochemical testing, and high-resolution cycle analysis, the Triassic lacustrine shale in the Ordos Basin was studied to confirm that periodic oscillations of the paleo-environment occurred at different timescales during the Triassic. On the millennial scale, increased obliquity induced enhanced transfer of heat and moisture to high latitudes, which then recharged continental aquifers, resulting in an increase in temperature, humidity, and levels of lakes in the mid-latitudes of the Northern Hemisphere. In contrast, decreased obliquity induced temperature and humidity reduction, followed by lake-level decline. Variations in eccentricity further regulated the magnitude of obliquity-forced paleo-environmental evolution. On the decadal–centennial scale, solar activity, including the 360–500 yr cycle I, 81–110 yr cycle II, and 30–57 yr cycle III, caused high-frequency oscillations of humidity and lake level. In the mid-latitudes of the Northern Hemisphere, intense (weak) solar activity promoted the decline (rise) in humidity and lake level. On the interannual scale, in the coastal area of western Panthalassa, El Niño-Southern Oscillation (ENSO)-like cycles also induced significant fluctuations in humidity and reducibility on a 2–8 yr scale. Whether complex paleo-environmental oscillations at different timescales occurred worldwide during the Triassic remains to be verified at other places. It is also noteworthy that high-frequency paleo-environmental oscillations in the Triassic stimulated algal blooms over a short period. The increase in rainfall caused by solar activity and ENSO-like cycles led to a frequent influx of nutrients into the Ordos Basin. The 30–57 yr cycle III induced red algae enrichment at intervals of decades. ENSO-like cycles also promoted algal bloom on 2–8 yr scale to form organic layers in lacustrine shale.

1. Introduction

The Triassic is considered a critical time interval in Earth's history, bounded by two phases of major mass extinctions and associated with an interval of supercontinent aggregation (Parrish, 1993; Preto et al., 2010; Liu et al., 2021a). The greenhouse climatic conditions and geochemistry of seawater during the Triassic are believed to offer an analogue for today's climate change and ocean scenarios (Preto et al., 2010; Corso et al., 2012). Reconstruction of the Triassic paleo-environmental evolution, therefore, is of immense significance for predicting future climate change and marine environmental evolution (Preto et al., 2010). In previous studies, changes in global climate caused by major geological events at both boundaries of the Triassic have been widely investigated (Tanner et al., 2004; Grasby et al., 2017; Percival et al., 2017; Thibodeau et al., 2016). Some other researchers were devoted to analyze the ecosystem recovery in the early Triassic following the end-Permian mass extinction through biodiversity investigations (Foster and Sebe, 2017; Martindale et al., 2019). However, the study on the Triassic paleo-environmental evolution has been relatively neglected (Galfetti et al., 2008; Preto et al., 2010). Given the lack of evidence on glaciations, older accounts largely characterized the Triassic was a “hot-house” world featuring a gradual, monotonous, long-term cooling trend (Preto et al., 2010; Kiessling, 2010). Recently, a few researchers have shown that paleo-environmental oscillation, represented by three cooler intervals,

---

* Corresponding author.
E-mail address: xikelai@upc.edu.cn (K. Xi).

https://doi.org/10.1016/j.palaeo.2022.111376
Received 1 September 2022; Received in revised form 22 December 2022; Accepted 23 December 2022

occurred during the Middle Triassic (Trotter et al., 2015). The global extreme humid climatic oscillation (the Carnian Pluvial Event) was also identified to have occurred during the late Triassic (Corso et al., 2018). The existence of these climate oscillations suggests that the Triassic paleo-environmental evolution was unstable.

Sedimentological studies have found that sedimentary cycles were extensively recorded in the Triassic strata. Alternate deposition of silt-rich units and dolomite-rich/mud-rich units forming meter-scale cycles has been commonly identified in the marine carbonate platform from Yangtze Platform (middle Triassic) (Liu et al., 2021a), lacustrine deposits from East Greenland (late Triassic) (Clemmensen et al., 1998), and terrestrial terminal alluvial plain from German Keuper Basin (late Triassic) (Hornung and Aigner, 1999). Centimeter-scale alterations of black shales and carbonate rocks/siltstones were also identified in the marine carbonate platform from Nanpanjiang Basin (early Triassic) (Galfetti et al., 2008), upper Anisian-Ladinian marine carbonate platform (middle Triassic) (Hinnov and Goldhammer, 1991), lacustrine deposits from East Greenland (late Triassic) (Clemmensen et al., 1998) and German Keuper Basin (late Triassic) (Reinhardt and Ricken, 2000). Cyclical sedimentary records in sediments are considered the result of periodic paleo-environmental evolution (Anderson and Dean, 1988; Clausing and Boy, 2000; Andrews et al., 2010). This further suggests that in addition to climate disturbances, periodic paleo-environmental evolution also occurred in the Triassic. In particular, high-frequency paleo-environmental fluctuations recorded by centimeter-scale sedimentary cycles may stably exist. However, the periodic timescales and driving factors of these complex paleo-environmental evolutions are not well understood. This limits our understanding of the characteristics and laws of paleo-environmental evolution in the Triassic.

Thick-bedded shales deposited in deep-lake areas provide an excellent case for sedimentary cycle identification and paleo-environment reconstruction. Petrographic analysis suggests that thickly-bedded shales from the Chang 7_3 sub-member have recorded different-scale sedimentary cycles. In this study, the timescales of the periodic evolution of the paleo-environment recorded by these sedimentary cycles were clarified. Thereafter, different driving factors and their forcing paleo-environmental evolution in the Triassic were identified. Moreover, the implication of the high-frequency paleo-environmental evolution for algal bloom in the Triassic is discussed.

2. Geological background

The Ordos Basin is a large multi-cycle cratonic basin in the western North China Block. In the late Triassic, it was located in the northern Paleo-Tethys region (Fig. 1A) at approximately mid-latitudes (Carroll et al., 2010). It is bound to the east by the Lvliang Mountain and Lishi Fault, to the west by the Helan Mountain, to the north by the Xing'an Mongolian orogenic belt and the Dengkou-tuoketuo Fault, and to the south by the Qinling orogenic belts and Huaibei flexure belt (Fig.1B).

During the sedimentation of the Triassic Yanchang Formation, which was affected by the Indosinian orogeny, a large-scale inland depression lake basin formed (Fu et al., 2020). During this period, a set of

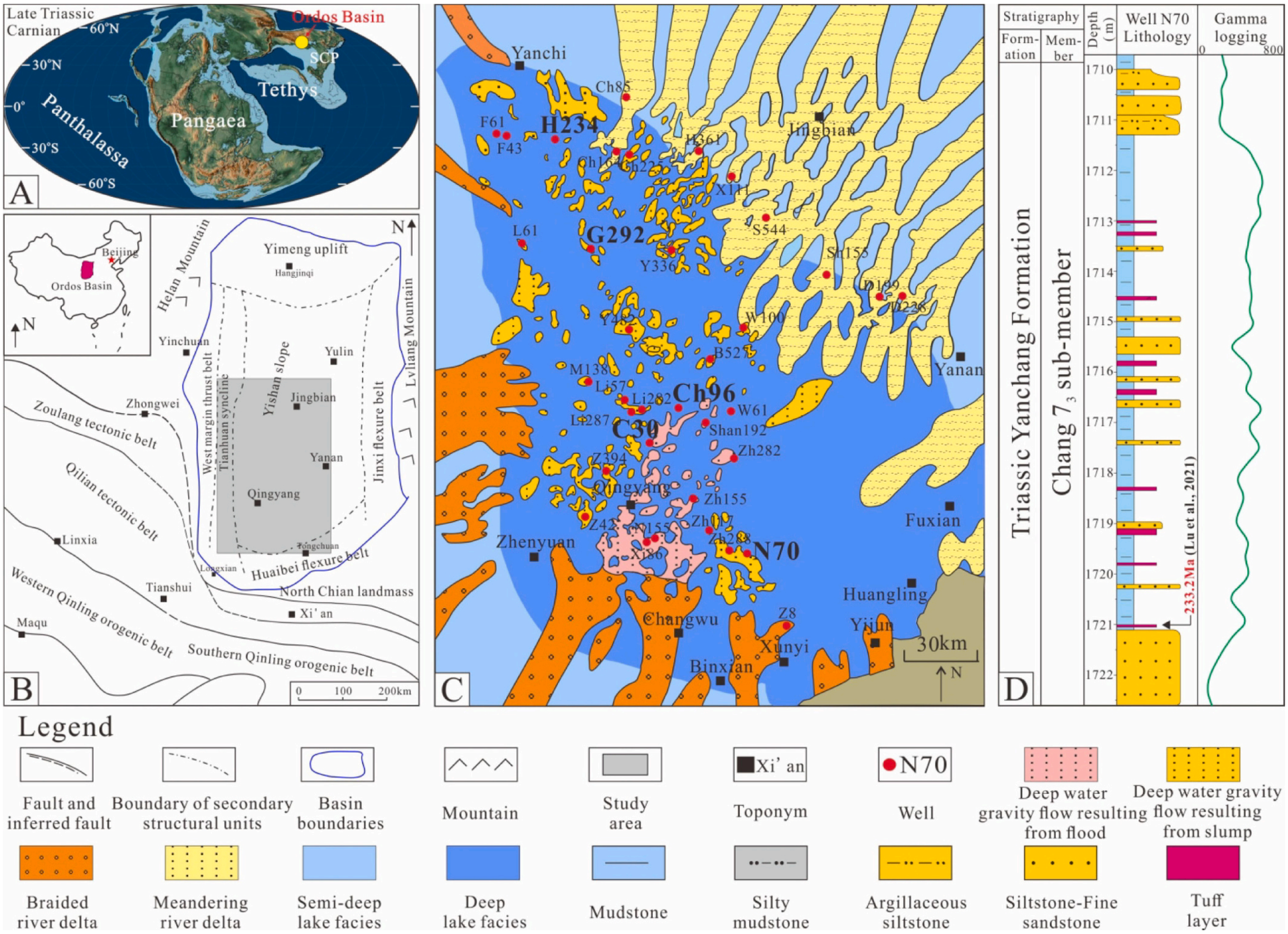

Fig. 1. A, Palaeogeographic map of the late Triassic (Scotese, 2014). B, tectonic location of the Ordos basin showing distribution of uplifts, flexure belts and orogenic belts (Zhou et al., 1995; Fu et al., 2018). C, plane distribution characteristics of sedimentary facies and Well sites in Chang 7_3 sub-member. D, stratigraphic development characteristics in Chang 7_3 sub-member. SCP- South China Plate.

terrigenous clastic rocks of mainly fluvial-lacustrine facies were deposited in the basin, which can be divided into 10 members: Chang 1 to Chang 10 (Fu et al., 2020). The Chang 7 member can be divided into three sub-members: Chang 7_1, Chang 7_2, and Chang 7_3. The studied Chang 7_3 sub-member with a thickness of 28–42 m is a shale-dominated formation at a burial depth of 1500–3000 m (Fig. 1B, C). At that time, the highest lake level was reached, inducing a large deep-lake area in the Ordos Basin (Fu et al., 2020). The thinly-bedded sandstones of gravity flow origin and the thickly-bedded shales mainly deposited in the deep-lake area (Liu et al., 2021b). According to the lithological description, the sandstones of gravity flow origin mainly occur on the top and bottom of the Chang 7_3 sub-member, while the thickly-bedded shales are steadily deposited between them (Fig. 1D). Tuff layers, with a thickness of 5–17 mm, were mainly identified in the thickly-bedded shale interval (Fig. 1D). In order to eliminate the interference of slump and flood deposits on cyclostratigraphy research, thickly-bedded shales that reflect the continuous deep-water environment were selected as the focus interval for this study.

Based on the zircon U–Pb dating of tuff layers, the thickly-bedded shales began to deposit during the late Triassic (approximately 233.2 Ma) (Lu et al., 2021). A relatively warm–humid paleoclimate can be identified during the sedimentary period of the Chang 7_3 sub-member (Fu et al., 2020). Thickly-bedded lacustrine shales were deposited during this period, with no sedimentary discontinuities (Zhang et al., 2016). This provides favorable conditions for sedimentary cycle identification and paleo-environmental reconstruction.

3. Materials and methods

Five major core holes (Well Ch96, N70, C30, G292 and H234) with continuous coring performed in the Chang 7_3 sub-member were selected in the Ordos basin. Logging data from these five Wells were used to identify the astronomical cycles in the Triassic. Hand-held X-ray fluorescence (XRF) analysis was finely performed on the continuous cores from Well Ch96. Bulk shale samples were collected from two key core holes (Well Ch96 and N70) for this research. Shale samples were first prepared for thin section and microscopic observation. Typical samples with clear and relatively flat laminar interfaces were selected for Advanced Mineral Identification and Characterization System (AMICS) analysis. Bulk shale samples with clear lamination characteristics were polished and conducted micro X-ray fluorescence spectroscopy (Micro-XRF) analysis. The above experimental analyses were performed at the Key laboratory of deep oil and gas, China University of Petroleum (East China).

Microscopic observation focus on the lamina type, thickness, and distribution. The fluorescence observation was used to identify the algae distribution. They were performed using a Zeiss microscope (Imaging-2 M). Mineral compositions in different types of lamina were quantitative statistics by AMICS analysis using Zeiss Crossbeam 550 FIB-SEM integrated with a Bruker EDS analysis system (X-Flasher Detector 430-M). Freshly prepared thin sections were carbon-coated and glued onto aluminum stubs. During AMICS analyses, the analyzed area was firstly scanned by backscattering (BSE). Then, analyzed area was automatically carried out mineral identification with High-Resolution EDS. AMICS analysis software and database were used to identify the boundaries of mineral. High resolution of boundary partition can reach to 20 μm.

The injection of volcanic ash induced the uranium anomaly in Chang 7_3 sub-member (Qiu et al., 2015), which reduced the sensitivity of gamma-ray data to identify the lithological variation. Therefore, the induction logging data were eventually selected to identify periodic changes in lithology and astronomical cycles. The induction logging data were confirmed to be the useful tool for achieving our purposes (Peng et al., 2020). For the original induction logging data from five selected Wells, long-term trends were removed to avoid distortion of low-frequency spectral peaks in the spectrum by using the "LOWESS" method to remove 35% weighted average in Acycle 2.3 software (Li et al., 2019). Then, Multitaper Method of Spectral Analysis (MTM analysis) and wavelet analysis based on the pre-processed induction logging data were performed in the thick-bedded shales from Chang 7_3 sub-member in order to identification of Milankovitch cycle. The frequency of statistically significant peaks (with confidence over 90%) in the spectrum can be identified. The signals of orbital parameters were extracted from the stratigraphic series using the Gaussian bandpass filter in the Acycle 2.3 software (Li et al., 2019). After that, the accumulation rates of the thick-bedded shale from Well Ch96 and N70 were obtained using correlation coefficient method (COCO/eCOCO) by Acycle 2.3 software.

The hand-held XRF analysis was used to obtain the relative content of different elements in shale cores. The element ratios were then used to reconstruct the paleo-environmental evolution controlled by orbital parameters. The handheld XRF instrument was carefully positioned on the slabbed clean surfaces of the drilled cores, with the beam (with a diameter of less than 1 cm) pointing downward. "Mining mode" was used to for a duration of 120 s to determine the major element oxides (SiO_2, Al_2O_3, Fe_2O_3, K_2O, CaO, MgO, and P_2O_5), and "Soil mode" was used for a duration of 150 s to determine the trace element concentrations (Mo, Zr, Sr, U, Rb, Th, Pb, Au, As, Hg, Li, Be, Sc, Se, V, Ni, Cr, Co, Mn, Ti, Cu, Zn, W, Ag, Pd, Cd, Sb, Cs, Te, Sn, Ba, Bi, Nb, and Cl). The concentrations of the elements and oxides were expressed in ppm. The relative standard deviation ranged from 0.21% to 8.2%, within the criteria of 10% for definitive data quality. The intervals between the testing points were about 10–20 cm.

Micro-XRF analysis was used to identify the sedimentary cycles in shales through continuous in-situ element testing on bulk core samples. The results of in-situ elemental analysis were further used for reconstruction of the high frequency paleo-environment evolution. Micro-XRF analysis was conducted using a Bruker M4 Tornado high-performance XRF spectrometer. Each sample was polished to enhance image resolution. The samples were then put into the sample compartment and horizontally aligned using a level gauge. Element scanning was done using a silicon drift detector with an acceleration voltage of 50 keV, a beam current of 800 mA. Rhodium was chosen as the target material for the X-ray lighter. The scanning rate was ~12 ms per point. The qualitative and quantitative characteristics of Na, K, Ca, Mg, Al, Si, Fe, S, Mn, Sr, Ti, V, Cr, Cu, Ni, Co, Sr, Ba and Mo were detected in this study. Each bulk shale sample was scanned for more than 8 h. The shale samples from N70 were about 10 cm in length, while the samples from Ch96 were from 2 to 5 cm in length. The analytical accuracy was 20 μm. Element distribution map was used to analyze the laminae types and their distribution characteristics. Due to the differences in element enrichment characteristics in different laminae, different types of laminae in the image will show different color after element stacking. Different types of laminae in the image of Micro-XRF analysis was then calibrated on the basis of microscopic observations. Finally, multi-scale cyclical sedimentary records can be determined by identifying the distribution characteristics of different types of laminae in the images of Micro-XRF analysis. After the elemental analysis of the bulk shale samples, a rectangular area perpendicular to the laminae was selected in each sample. Quantitative analysis results of elemental content in this rectangular region were then extracted. The length of the rectangular region spans the entire sample. Setting a certain width is to ensure the element content of each position in the direction perpendicular to laminae can be obtained by the data of multiple points on average. The scanning step in the direction perpendicular to laminae is around 25–35 μm in different shale samples. The obtained geochemical parameters, such as REDOX index (Mo/Ti ratio) and humidity index (C value), were used to further analyze the high frequency paleo-environment evolution. C value $= \Sigma (Fe + Mn + Cr + Ni + V + Co)/\Sigma (Ca + Mg + K + Na + Sr + Ba)$, the element in the formula represents the content of each corresponding element (Qiu et al., 2015).

The geochemical parameters obtained from the micro-XRF analysis were de-trended using the Past software (Hammer et al., 2001). Based on

Fourier transform, Acycle 2.3 software was also used to perform spectral and wavelet analysis on the pre-processed data. Then the frequency of statistically significant peaks (with confidence over 90%) in the spectrum can be identified. Match the results of spectrum analysis and those of continuous wavelet analysis. The sedimentary cycles caused by high frequency paleo-environment evolution in Chang 7_3 sub-member can be determined. The identified thickness of sedimentary cycles from multiple samples were compared to select the thickness cycles that are present in all samples. The thickness of the selected sedimentary cycles was then divided by the corresponding accumulation rates in order to obtain the timescale of each sedimentary cycle. These timescales were used to analyze the driving factors of paleo-environment evolution. The obtained sedimentary cycles were then performed filtering analysis using the Gaussian bandpass filter in the Acycle 2.3 software (Li et al., 2019). Filtering results were matched with the results of paleo-environment reconstruction in order to analyze the control of driving factors on high frequency paleo-environment evolution in the Triassic.

4. Results

4.1. *Sedimentary characteristics of Chang 7_3 sub-member during the late Triassic*

The laminar structure was mainly developed in lacustrine shales in the Chang 7_3 sub-member. Three types of lamina were identified as: silt-grained felsic laminae (SSFL), tuff-rich laminae (TRL), and organic-rich laminae (ORL) (Figs. 2A, B). K-feldspar was dominant in the SSFL, with a content of 70% (Fig. 2C); the rest are almost quartz and plagioclase, with contents of 7.24% and 5.53%, respectively (Fig. 2C). The TRL is mainly composed of mixed layers of smectite/illite, which is approximately 80% of its content (Fig. 2D); minor organic matter and pyrites could also be mixed in the TRL (Fig. 2D). Compared to the TRL, mixed layers of smectite/illite in the ORL decreased to 52% in content, whereas organic matter and pyrite contents increased (Fig. 2D). Alternate deposition of these three types of lamina constituted two types of shale in the Chang 7_3 sub-member. Laminated shale (SSFL + ORL) consists of interbedded SSFL and ORL (Fig. 2A), whereas laminated shale (TRL + ORL) is composed of interbedded TRL and ORL (Fig. 2B).

The vertical distribution of different types of shale and lamina appears to exhibit multi-scale cyclicity. At the meter-scale, different types of shale are periodically deposited in large quantities. The vertical distance between the locations where the same types of shales began to deposit massively was approximately 2 m (Fig. 3A). At the millimeter-micron scale, the thickness of the same type of lamina generally changes cyclically (Fig. 3B), and two types of lamina are usually alternately deposited (Figs. 2A, B). Cyclic changes in laminar types always occur within approximately 0.95–2.6 mm. Cyclical sedimentary records are considered the result of periodic paleo-environmental evolution (Anderson and Dean, 1988; Clausing and Boy, 2000; Andrews et al., 2010). The multi-scale sedimentary cycles in the Chang 7_3 sub-member suggest that periodic paleo-environmental fluctuations of the late Triassic occurred on different timescales.

4.2. *Identification of the Milankovitch cycle*

Tectonic activity was relatively stable during the sedimentary period of the Chang 7_3 sub-member of the Ordos Basin (Fu et al., 2018). In this context, periodic lithological variations on a meter scale are likely controlled by the Milankovitch cycle (Sageman et al., 1997; Kuiper et al., 2008). In deep-water environments, regular changes in lithology may be difficult to accurately identify with the naked eye (Wu et al., 2011). Logging data were then used to identify the possible sedimentary cycles at the meter scale recorded in the Chang 7_3 sub-member. Given the abnormal uranium content induced by the injection of volcanic ash (Qiu et al., 2015), the identification of lithological variation using gamma logging data were affected. Therefore, induction conductivity logging (CILD) was selected to identify periodic changes in lithology. Spectral and wavelet analyses showed that sedimentary cycles were clearly recorded in the Chang 7_3 sub-member (Fig. 4). In Well Ch96, the thickness ratio of sedimentary cycles with a confidence coefficient greater than 99% in the MTM analysis was 5.162:2.547: 5.162:2.547:2.054:1.224:1 (Fig. 4). This is similar to the theoretical period ratio of the orbit parameters (5.362-eccentricity:2.560-obliquity:2.015-obliquity:1.195-precession:1-precession) in the late Triassic

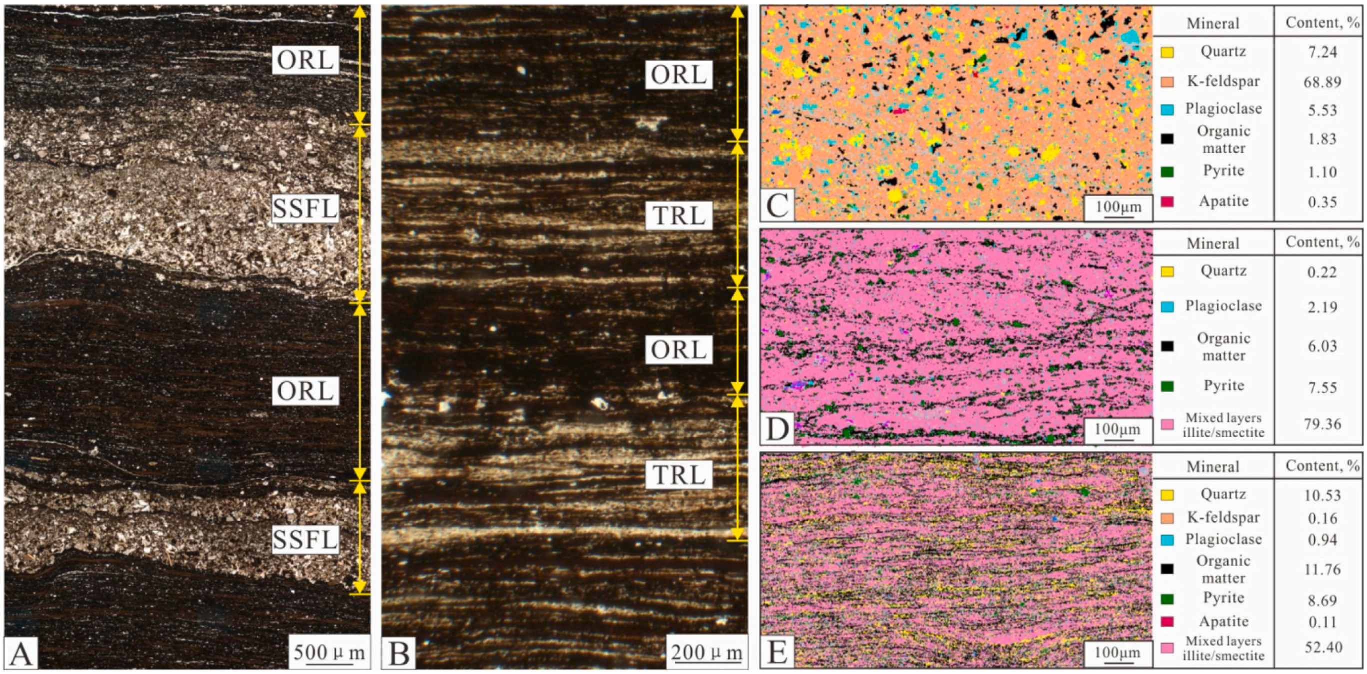

Mineral	Content, %
🟨 Quartz	7.24
🟧 K-feldspar	68.89
🟦 Plagioclase	5.53
⬛ Organic matter	1.83
🟩 Pyrite	1.10
🟥 Apatite	0.35

Mineral	Content, %
🟨 Quartz	0.22
🟦 Plagioclase	2.19
⬛ Organic matter	6.03
🟩 Pyrite	7.55
🟪 Mixed layers illite/smectite	79.36

Mineral	Content, %
🟨 Quartz	10.53
🟧 K-feldspar	0.16
🟦 Plagioclase	0.94
⬛ Organic matter	11.76
🟩 Pyrite	8.69
🟥 Apatite	0.11
🟪 Mixed layers illite/smectite	52.40

Fig. 2. Petrological characteristics of lacustrine shales in the Chang 7_3 sub-member. A, petrographic images of ORL and SSFL under plane-polarized light. B, petrographic images of ORL and TRL under plane-polarized light. C, AMICS analysis results of SSFL (Lin et al., 2022). D, AMICS analysis results of TRL. E, AMICS analysis results of ORL (Lin et al., 2022). SSFL- silt-sized felsic laminae, TRL- tuff-rich lamina, ORL- organic-rich lamina.

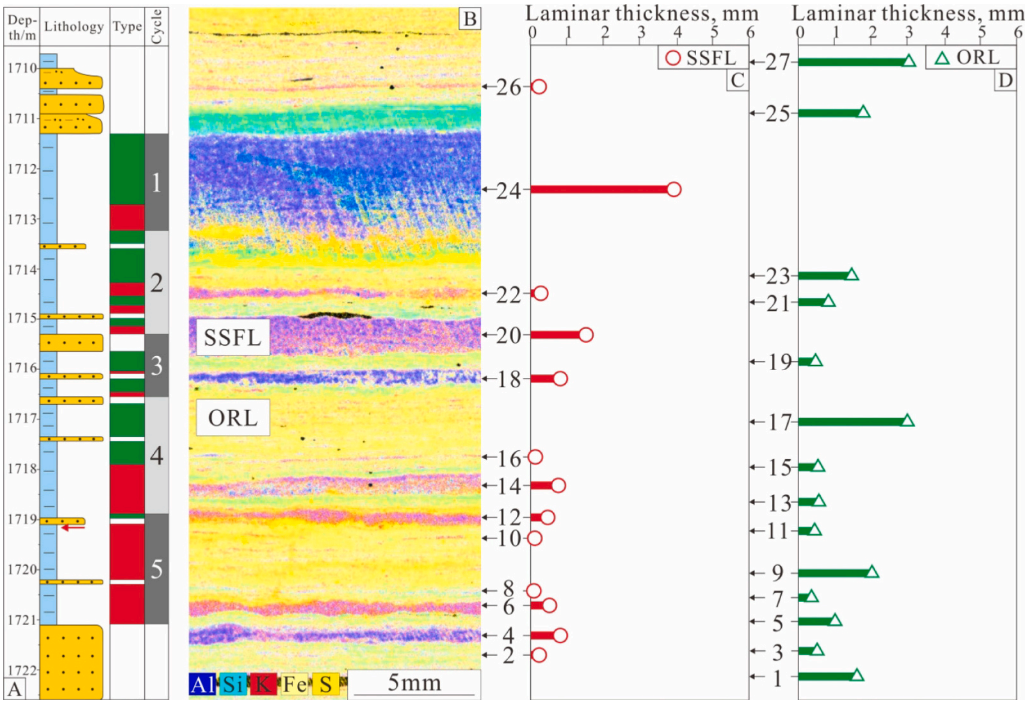

Fig. 3. Multi-scale sedimentary cycles in Chang 7_3 sub-member. A, different types of shale deposited in large quantities periodically on the meter-scale. Each number from 1 to 5 indicates the transition of the area of main deposit laminated shale (TRL + ORL) to the area of main deposit laminated shale (SSFL+ORL). B, characteristics of different types of lamina and their thickness after micro-XRF analysis. C, the variation of SSFL thickness from bottom to top in panel B; D, the variation of ORL thickness from bottom to top in panel B; panel C and D show that the thickness of the same type of lamina generally changes cyclically on the millimeter scale. Green bars in panel A indicate the laminated shales (TRL + ORL). Red bars in panel A indicate the laminated shales (SSFL+ORL). The red arrow in panel A indicate the position of the samples in panel B. SSFL- silt-sized felsic lamina, ORL- organic-rich lamina. (For interpretation of the references to colour in this figure legend, the reader is referred to the web version of this article.) (For interpretation of the references to colour in this figure legend, the reader is referred to the web version of this article.)

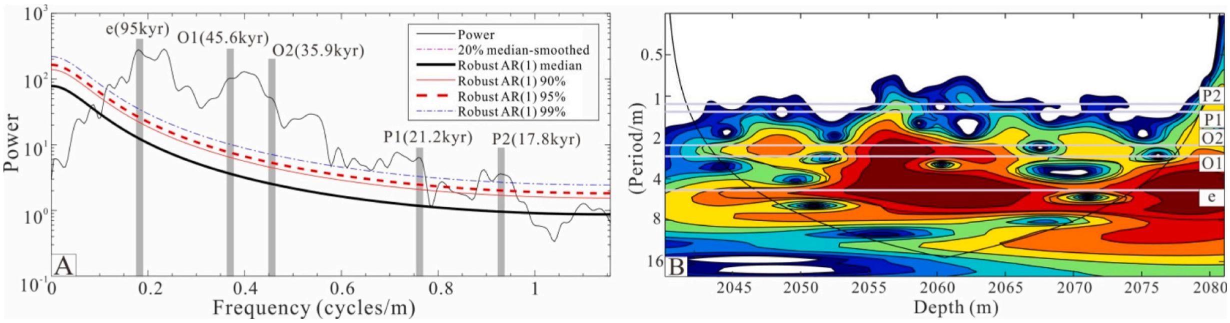

Fig. 4. Spectral (A) and wavelet (B) analysis of induction logging data of the Chang 7_3 sub-member.

(Berger et al., 1989). In other wells, such as N70, C30, G292, and H234, the thickness ratios of lithological cycles on a meter scale, which are similar to the theoretical period ratio of orbit parameters, can also be identified (Table 1). This further suggests that eccentricity, obliquity, and precession were stably recorded in the thick-bedded lacustrine shales in the Chang 7_3 sub-member.

Correlation coefficient (COCO) analysis, after Milankovitch cycle identification, was conducted to calculate the accumulation rates of the Chang 7_3 sub-member (Figs. 5A, B). The accumulation rate of 5.2 cm/kyr was higher than the 99% confidence coefficient in Well Ch96 (Fig. 5A). Based on eCOCO analysis, the accumulation rate of thickly-bedded shales was mainly 5.2 cm/kyr, whereas some shales with approximately 4.5 cm/kyr accumulation rate were distributed at the bottom of the Chang 7_3 sub-member (Fig. 5C). Another well, N70, was selected to verify the accuracy of the calculated accumulation rates in the Chang 7_3 sub-member. The accumulation rate of thick-bedded shales in N70 is relatively stable at approximately 5.4 cm/kyr with higher than 99% confidence coefficient (Fig. 5B) (Lin et al., 2022). The accumulation rate of shales at the bottom of Chang 7_3 sub-member decreases to approximately 4.0 cm/kyr (Fig. 5D). Therefore, the accumulation rates of shales in the Chang 7_3 sub-member were in the 4.0–5.4 cm/kyr range. Zhao et al. (2020) used ID-TIMS for accurate zircon dating of tuffs in the Chang 7_3 sub-member, based on which they conducted astronomical tuning, and the deposition rate of thick-bedded shales in the southern Ordos Basin was estimated at 4.0–4.9 cm/kyr. The deposition rate calculated in this study was quite similar to that reported by Zhao et al. (2020). Therefore, the calculated deposition rate of thickly-bedded shales in the Chang 7_3 sub-member from Wells Ch96 and N70 should be convincing.

Table 1
Thickness ratios of sedimentary cycles identified in different Wells in the Chang 7_3 sub-member.

Well	Thickness ratios of sedimentary cycles identified in CILD series
Ch96	5.162 (e): 2.547 (O1): 2.054 (O2): 1.224 (P1): 1 (P2)
N70	5.139 (e): 2.569 (O1): 2.056 (O2): 1.171 (P1): 1 (P2)
C30	5.199 (e): 2.600 (O1): 2.079 (O2): 1.195 (P1): 1 (P2)
G292	5.594 (e): 2.452 (O1): 2.000 (O2): 1.178 (P1): 1 (P2)
H234	5.324 (e): 2.626 (O1): 2.010 (O2): 1.173 (P1): 1 (P2)

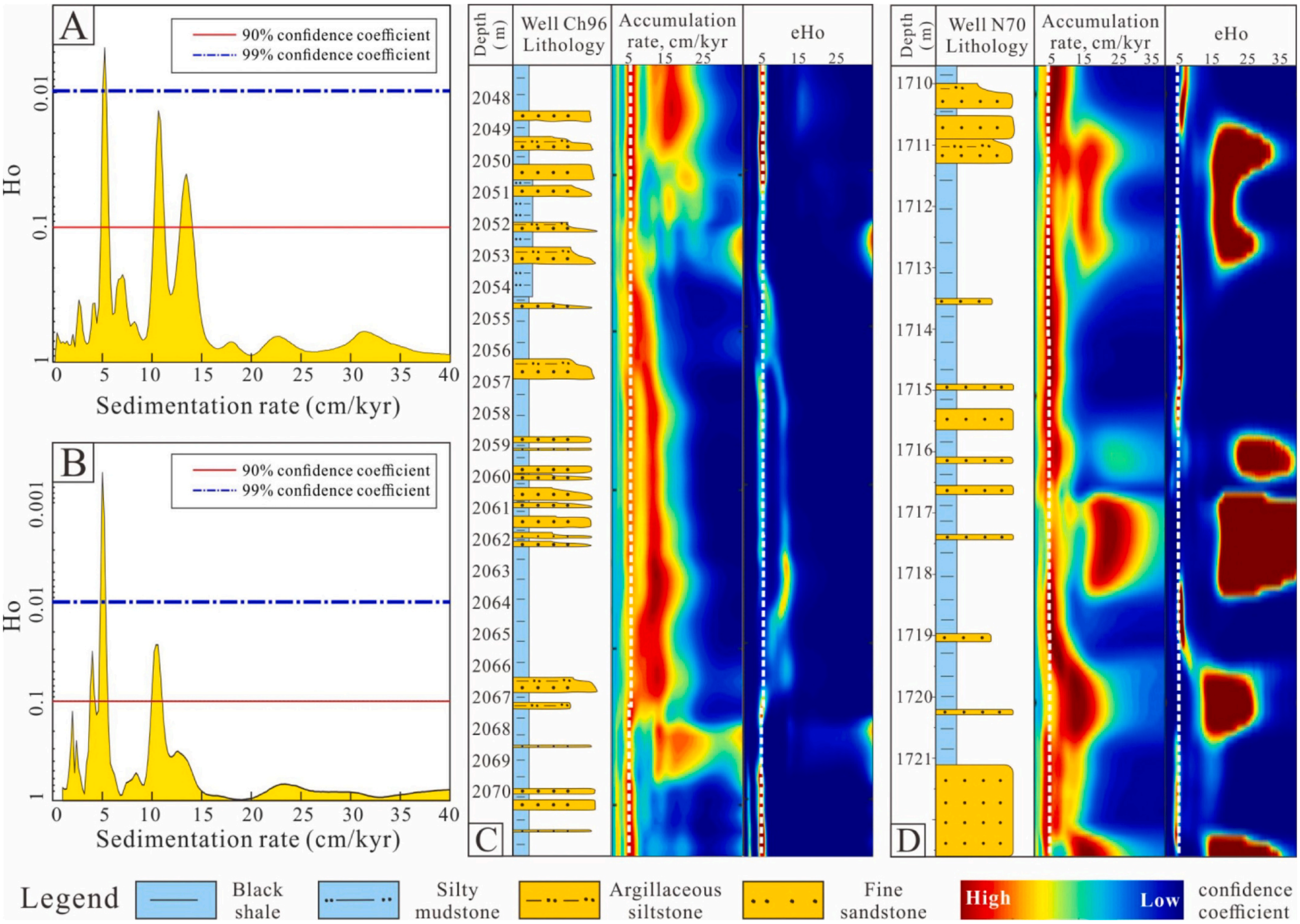

Fig. 5. Accumulation rates of thick-bedded shales in Chang 7_3 sub-member. A, average deposition rate of Chang 7_3 sub-member from Well Ch96 using COCO method analysis (accumulation rate test range: 1–40 cm/kyr; step: 0.1 cm/kyr). B, average deposition rate of Chang 7_3 sub-member from Well N70 using COCO method analysis (accumulation rate test range: 1–40 cm/kyr; step: 0.1 cm/kyr) (Lin et al., 2022). C, accumulation rates of thick-bedded shales in Chang 7_3 sub-member from Well Ch96 using eCOCO method analysis (accumulation rate test range: 1–40 cm/kyr; step: 0.1 cm/kyr; sliding window size: 10 m). D, accumulation rates of thick-bedded shales in Chang 7_3 sub-member from Well N70 using eCOCO method analysis (accumulation rate test range: 1–40 cm/kyr; step: 0.1 cm/kyr; sliding window size: 6 m) (Lin et al., 2022). The white dotted line within in the eCOCO result is accumulation rates according to the 95-kyr tuning of the statistically cycles in Well Ch96 and N70.

4.3. Identification of solar activity and El Niño-Southern Oscillation-like cycles

On centimeter-micron scales, cyclic variations in laminar composition and thickness may record the solar activity cycle, atmospheric circulation cycle, or seasonal cycle (Ripepe et al., 1991; Shunk et al., 2008; Li et al., 2018a). The fine identification of these small-scale sedimentary cycles is key to exploring the periodic evolution of the paleoenvironment over a short timescale. Variability in varve thickness and gray value was used to identify the sedimentary cycles at centimeter-micron scales (Lückge et al., 2001). In the Chang 7_3 sub-member, however, the varve does not exist in view of the accumulation rate and the thickness of the laminar couplets (Figs. 2A, B; 5). The shales with a high organic matter content also resulted in a black core as a whole and no obvious difference in gray value. The two traditional methods for identifying small-scale sedimentary cycles are ineffective. In situ elemental analysis indicated that the aluminium (Al) content was significantly different among the three types of lamina, which was highest in SSFL, followed by TRL and ORL (Fig. 6A). The activity of Al is poor and its content does not significantly change during diagenetic evolution (Hayashi et al., 1997). Therefore, cyclic variation of Al content was used to identify the sedimentary cycles at centimeter-micron scales. Micro-XRF analysis was conducted to obtain the distributions of Al content along the vertical laminar direction in different core samples (Fig. 6B). Cyclic variation of Al content on the centimeter-micron scale was obvious after spectral and wavelet analyses (Figs. 6C, D). In Well N70, the thickness of sedimentary cycles is stably distributed in approximately 16.9–27.8 mm, 4.1–5.9 mm, 1.5–2.8 mm, and 0.1–0.5 mm, respectively (Appendix A). The short length of the cores in Well Ch96 results in the centimeter-scale sedimentary cycles are difficult to identify (Appendix A). The cycles in millimeter-micron scales, however, can be stably recorded in Well Ch96, including 4.4–5.9 mm, 1.6–3.2 mm, and 0.1–0.4 mm in thickness (Appendix A). According to the accumulation rates of shales in the two wells, the timescales of these small-scale sedimentary cycles are steadily distributed in approximately 360–500 yr (cycle I), 81–110 yr (cycle II), 30–57 yr (cycle III), and 2.0–8.0 yr (cycle IV), respectively (Appendix A).

The timescales of cycles I–III are quite similar to those of the solar activity cycles. Classical solar activity cycles include the Schwabe quasi-cycle (~11 yr), Hale quasi-cycle (~22 yr), Gleissberg quasi-cycle (~88 yr), and Suess quasi-cycle (~208 yr) (Dicke, 1979; Damon and Sonnett, 1991; Hoyt and Schatten, 1998). Furthermore, solar activity cycles were confirmed to possess other quasi-cycles, including ~30–50 yr cycle, ~350–500 yr cycle, ~1000 yr cycle, and ~ 2241 yr cycle (http://pubs.

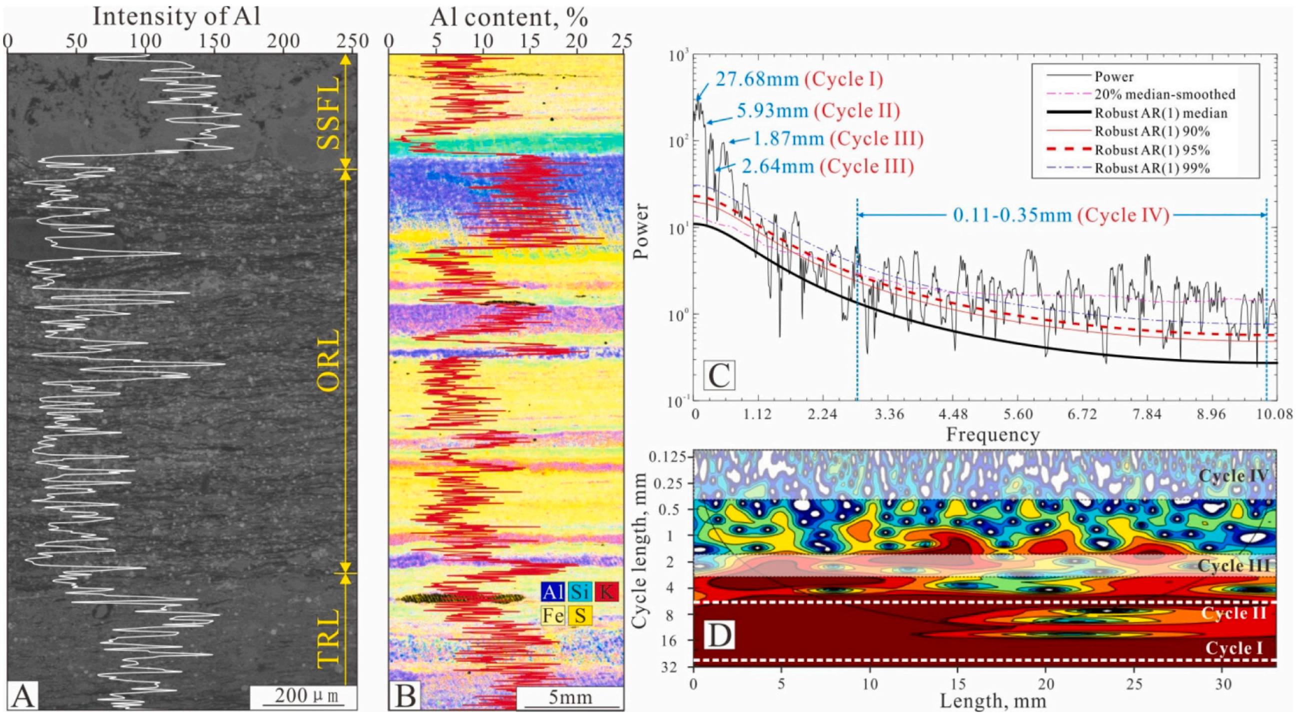

Fig. 6. A, Difference of Al content in different laminae after EDX analysis. B, Al content distribution along the vertical laminar direction after Micro-XRF analysis. C, spectral analysis of Al content in shale from Well N70, 1719.2 m. D, wavelet analysis of Al content in shale from Well N70, 1719.2 m. SSFL- silt-sized felsic lamina, TRL- tuff-rich lamina, ORL- organic-rich lamina.

usgs.gov/fs/fs-0095-00/fs-0095-00.pdf; Damon and Sonnett, 1991; Li et al., 2004; Yin et al., 2007; Zhao and Feng, 2015; Ma et al., 2021). Therefore, the stable cycles of 360–500 yr (cycle I), 81–110 yr (cycle II), and 30–57 yr (cycle III) should belong to solar activity cycles (Appendix A).

The timescales of cycle IV are most comparable to the present-day El Niño-Southern Oscillation (ENSO) cycle. Presently, the ENSO phenomenon has occurred irregularly for approximately 2–7 years (Shunk et al., 2008), which mainly show the periodicity of 2.1–2.85 yr, 3.0–3.6 yr, 4.0–5.5 yr, and 7 yr (Table 2). However, in band 0.11–0.35 mm, there are at least 20 peaks (Fig. 6C), which are much more than modern ENSO periods (Table 2). Some of the peaks in band 0.11–0.35 mm may be stochastic noise signals. In order to confirm that the signals of ENSO cycles are included in cycle IV, we further obtain the distribution of Al content by line scanning of energy spectrum (scanning step is 1 μm) and conduct the evolutionary spectral analysis (Figs. 7A-C). Combined with the sedimentation rates listed in Fig. 5, the timescales of cyclicities of Al contents are 2.0–2.6 yr, 3.5 yr, 4.2 yr and 7.0 yr (Fig. 7B), which are very similar to the modern ENSO periods (Table 2). In particular, there is also a good matching relationships between the filtering results of Al content cycles in 2–7 yr and the micron-scale sedimentary cycles in shales (Fig. 7D-E). One cycle of Al content includes one organic-matter layer and on clay-mineral layer (Fig. 7D-E), which proves that the interannual sedimentary cycles related to ENSO cycles are recorded in shales.

Table 2
Reconstruction of the timescales of modern ENSO cycles.

Time frame	Samples	Locations of the samples	Timescale of ENSO cycles	References
From 1870 to 2008	Niño 3.4 sea surface temperature (SST) time series	/	2.1–2.8 yr, 3.6 yr, 5.0–5.5 yr	Du et al., 2021
Last 600 years	Lacustrine sediments	Southern Chilean	2.4 yr, 3.0–3.2 yr, 4.4 yr	Fagel et al., 2008
~15,000-year record	Lacustrine sediments	Southwestern Ecuador	3–3.5 yr, 4–4.25 yr, 4.5–6 yr, 6.5–8 yr	Rodbell et al., 1999
Past 9000 years	Marine sediments	Southern California	2.3 yr, 4.3 yr, 5.9 yr	Du et al., 2021
14,700–17,150 year BP	Stalagmite	China	2.1–2.5 yr, 3.5 yr, 4.5–5 yr, 7 yr	Kong et al., 2003
From 1950 to 2006	Observational data of storm activity	Atlantic	2.4–2.85 yr, 3.5 yr, 4.5–5.5 yr	Kane, 2006
2100 year BP record	Marine varved sediments	British Columbia	3.6 yr	Dean and Kemp, 2004

In order to rule out the occasionality of our conclusion, we have selected another shale sample at the depth of 2055.55 m in Well Ch96 and identified the interannual sedimentary cycles related to ENSO cycles. Five areas are selected in this sample to explore if the sedimentary cycles related to ENSO-like cycles are stably recorded in shales (Fig. S1). We finally find that, in the five selected areas, (1) the timescales of cyclicities of Al contents are 2.1–2.8 yr, 3.0–3.7 yr, 4.3–5.4 yr and 7.1–8.0 yr (Fig. S2-S6) which are also similar to the modern ENSO periods (Fig. S2-S6 and Table 2); (2) the good matching relationships occur between the filtering results of Al content cycles in 2–7 yr and the micron-scale sedimentary cycles in shales (Fig. S2-S6); (3) One cycle of Al content also includes one organic-matter layer and on clay-mineral layer (Fig. S2-S6). Finally, we believe that the interannual sedimentary cycles are actually developed in the thickly-bedded shales from Chang 7_3 sub-member in Ordos Basin.

However, the configurations of the land and sea during the Triassic and the present are different (Scotese, 2014), so it is uncertain whether the ENSO effect existed during the sedimentary period of the Chang 7_3 sub-member. Given the reported timescales of sedimentary cycles in geological history, it is noteworthy that cycles of 2–7y were stably

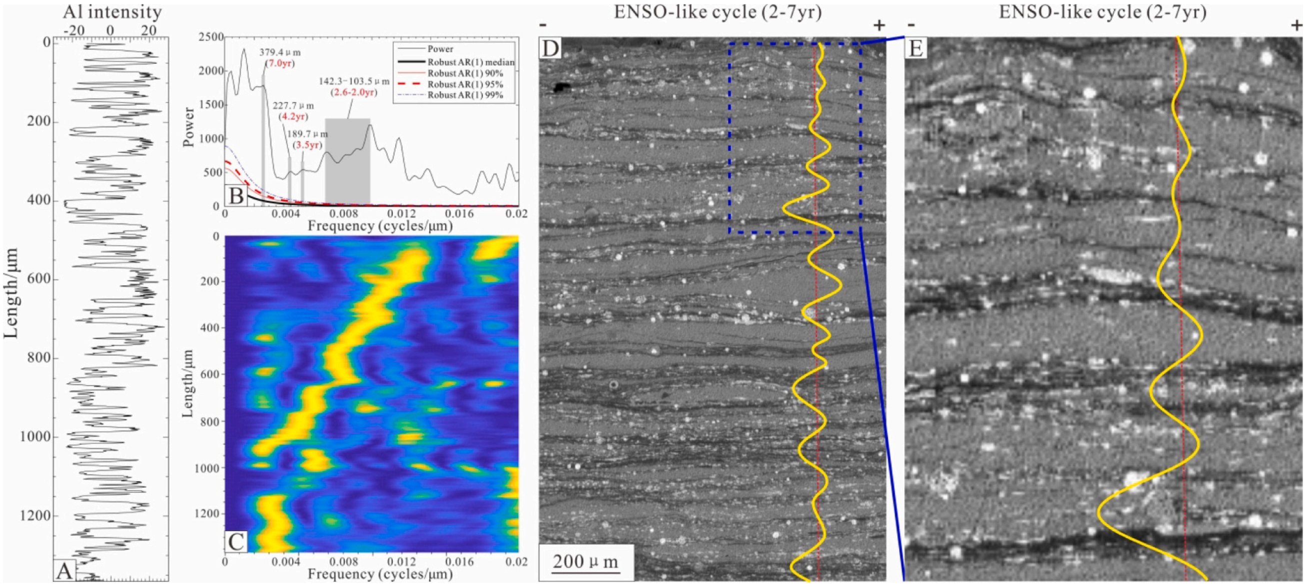

Fig. 7. Spectral analysis of Al content and filtering results of Al content cycles in 2–7 yr in shale sample at the depth of 1719.2 m from Well N70. A, distribution of Al intensity obtaining from line scanning by energy spectrum after de-trending analysis; B, MTM power spectrum of Al intensity distribution; C, evolutionary power spectrum of Al intensity was calculated using a 400 μm running window with a 1.93 μm step. D, microscopic features of shales under SEM and the filtering results of Al content cycles in 2–7 yr (Gaussian filter, passband: 0.00615 ± 0.0035 cycles/μm); E, microscopic features and the filtering results of Al content in the dotted box in panel D.

recorded from the Mesoproterozoic to the Holocene (Ripepe et al., 1991; Cooper et al., 2000; Baldwin et al., 2001; Park and Fürsich, 2001; Shunk et al., 2008; Andrews et al., 2010; Tang et al., 2014). Therefore, the 2–7 yr cycle was believed to have existed in the Triassic and was named the ENSO-like cycle in this study.

5. Discussion

5.1. Astronomical forcing of paleo-environmental evolution

Cyclic variation of the orbital parameters cause the changes of in astronomical insolation, which further results in the cyclic evolution of

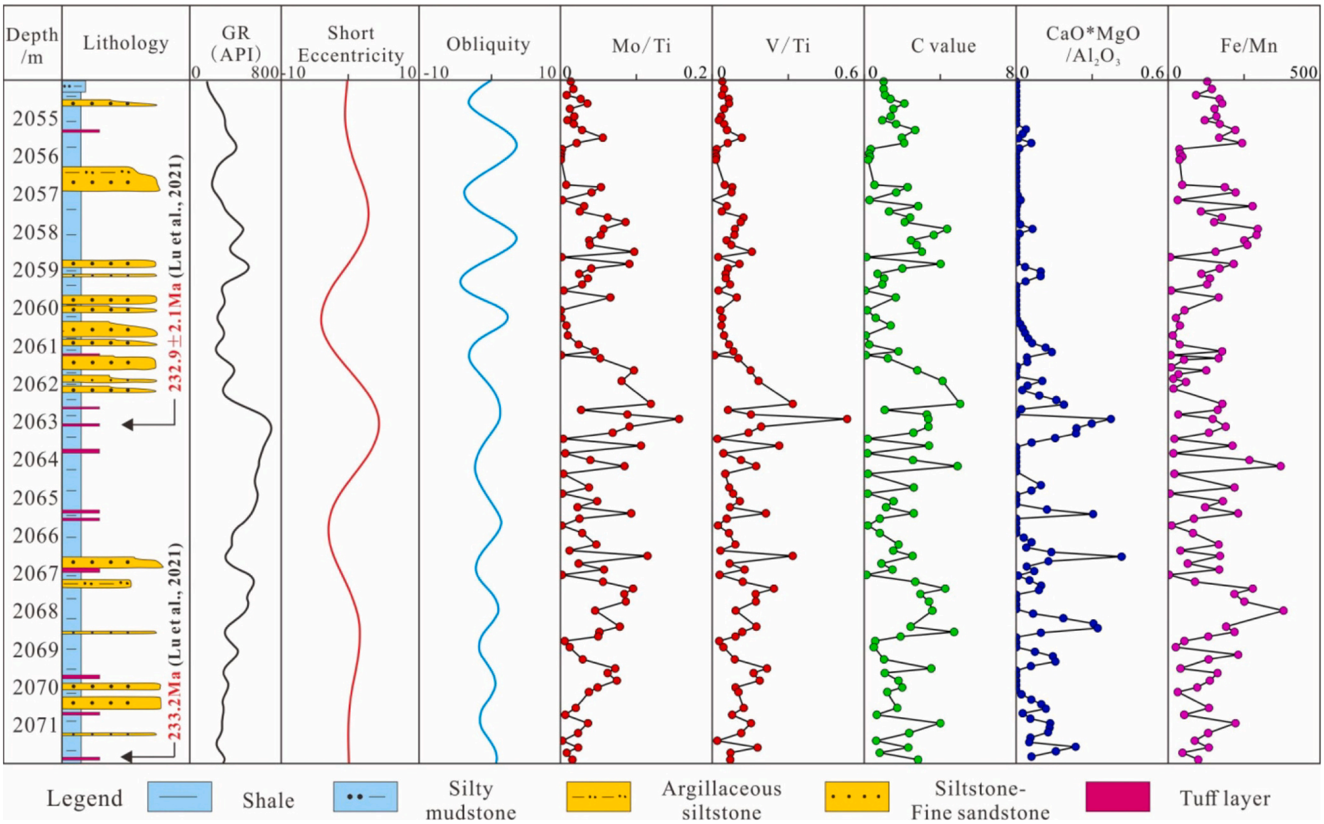

Fig. 8. Orbital-forced periodic paleo-environmental evolution during the late Triassic in Ordos Basin.

global climate (Wu et al., 2011; Huang et al., 2021). The strong obliquity signal in the CILD series may further indicate the significant influence of obliquity-forced paleo-environmental evolution during the late Triassic (Fig. 4). Obliquity mainly controls the variation in solar insolation at mid-high latitudes (Wu et al., 2000), which affects middle- to high-latitude atmospheric circulation and dominates the poleward fluxes of heat, moisture, and precipitation (Raymo and Nisancioglu, 2003; Huang et al., 2021). During the late Triassic, the Ordos Basin was located at approximately middle latitudes in the northern hemisphere (Carroll et al., 2010). The paleo-environmental fluctuation identified in the Ordos Basin corresponded well with the variation in obliquity (Fig. 8). Obliquity-forced sedimentation can also be identified in the Triassic South China Plate (Fig. 1A) (Liu et al., 2021a). This demonstrated that significant obliquity-forced paleo-environmental evolution occurred in mid-latitudes during the late Triassic. When obliquity increases, insolation increases in the mid-high latitudes of the Northern Hemisphere (Wu et al., 2000; Liu et al., 2019). The transfer of heat and moisture to high latitudes was enhanced during this process (Li et al., 2016; Huang et al., 2021). The increase in insolation and moisture transmission causes the temperature and humidity to increase in the Ordos Basin, which is supported by the increase in the C value and $CaO^{*}MgO/Al_2O_3$ (Qiu et al., 2015; Fu et al., 2018). Given the lack of glaciations during the Triassic, water mass mainly exchanges between groundwater and ocean reservoirs via climatic mediation (Li et al., 2016). In this context, the poleward flux of moisture recharges the continental aquifer when obliquity increases, thereby increasing the levels of lakes (Li et al., 2018b; Zhang et al., 2022). This is exactly supported by the increase in the Fe/Mn, Mo/Ti, and V/Ti ratios in the Ordos Basin (Fig. 8) (Brucker et al., 2011; Naeher et al., 2013; Nambiar et al., 2022). When obliquity decreases, a reduction in insolation and moisture transmission results in a decrease in temperature and humidity, followed by a decline in lake level. The decrease in Fe/Mn, Mo/Ti, and V/Ti ratios in coherence with the reduction in C value and $CaO^{*}MgO/Al_2O_3$ confirmed obliquity-forced paleo-environmental changes (Fig. 8) (Brucker et al., 2011; Naeher et al., 2013; Qiu et al., 2015; Fu et al., 2018; Nambiar et al., 2022).

In addition to obliquity-forced insolation variations, the change in eccentricity also affects solar insolation in the Northern Hemisphere. The in-phase increase in eccentricity and solar insolation occurs in the Northern Hemisphere and vice versa (De Boer et al., 2014). When obliquity reaches the maximum, the overlap of high eccentricity is likely to further increase solar insolation in the Northern Hemisphere. Compared with the overlapping period of maximum obliquity and minimum eccentricity, the humidity, temperature, and lake-level rose to the higher levels when the maximum obliquity and maximum eccentricity overlapped (Fig. 8). The variation in eccentricity, therefore, will further regulate the obliquity-forced paleo-environmental evolution during the late Triassic.

5.2. Solar activity and ENSO-like forcing of paleo-environmental evolution

In previous studies, solar activity and ENSO-like cycles have been identified in deep-time geological records (Table 3); however, they have not been reported in the Triassic (Table 3). The thickly-bedded shales from the Chang 7_3 sub-member recorded clear signals of solar activity and ENSO-like cycles during the late Triassic. With the background of orbital-forced paleo-environmental evolution, solar activity and ENSO-like cycles steadily existed (Appendix A) and further induced high-frequency paleo-environmental oscillations. The superposition of various driving factors resulted in a complex paleo-environmental evolution during the Triassic.

In this study, the rock composition (Al content) revealed variations of 360–500 yr, 81–100 yr, and 30–57 yr periodicities (Appendix A). It provided favorable evidence that the timescales of the solar activity cycle may have remained stable throughout geological history (Milana and Lopez, 1998; Andrews et al., 2010). Small changes in insolation controlled by the solar activity cycles can be amplified to a level sufficient to produce changes in weather and climate (Van Geel et al., 1999; Tian et al., 2021). When the number of sunspots increase, intense solar activity leads to an increase in solar insolation on the Earth's surface (Gray et al., 2010; Tian et al., 2021). The intense solar magnetic field during this period shields the Earth from cosmic rays (Lucio, 2005), thereby reducing cloud cover (Carslaw et al., 2002; Bal and Bose, 2010). Increased solar insolation and reduced cloud cover eventually lead to a warm–arid climate, followed by a decline in the levels of lakes (Magny et al., 2010; Song et al., 2015). In contrast, when the numbers of sunspots decrease, weak solar activity results in low solar insolation on the Earth's surface and high cloud cover, thereby inducing a cool–wet climate and increasing the levels of lakes (Magny et al., 2010; Song et al., 2015). In the Ordos Basin, humidity and reducibility also revealed variations of 360–500 yr, 81–110 yr, and 30–57 yr periodicities, which is supported by the spectral analysis of the C value and Mo/Ti ratio (Appendix A). This confirmed that solar activity controlled the paleo-environmental evolution during the late Triassic. In-phase variation of the C value and Mo/Ti ratio occurs, but they have obvious inverse phase relationships with Al content (Fig. 9). Al content enhancement corresponds to the massive deposition of silt-rich sediments (SSFL), whereas clay-rich sediments (ORL) were deposited when Al content decreased (Fig. 9). Combined with the change in Mo/Ti ratio, frequent variations in sediment grain size suggest lake-level fluctuations in the Ordos Basin (Bourget et al., 2010; Brucker et al., 2011; Tombo et al., 2015). Therefore, the C value and Mo/Ti ratio synchronously decrease, coherently depositing silt-rich sediments (Fig. 9), suggesting a decrease in humidity

Table 3
Solar activity and ENSO-like cycles identified in deep-time geologic records.

Cycle	Proterozoic era			Paleozoic						Mesozoic			Cenozoic	
	Pt1	Pt2	Pt3	Є	O	S	D	C	P	T	J	K	E	Q+N
2241 yr														●
~1000 yr														●
350–500 yr							●					●		●
~210 yr												●		●
~88 yr							●	●			●	●	●	●
30–50 yr							●	●	●		●	●	●	●
~22 yr		●	●					●				●		●
~11 yr	●	●	●				●	●			●	●	●	●
2–7 yr		●					●				●	●	●	●

The black filling cycles indicated the cycles were identified. Pt1-Paleoproterozoic: Li et al., 2018a; Pt2- Mesoproterozoic: Tang et al., 2014; Pt3- Neoproterozoic: Li et al., 2018a; D- Devonian: Andrews et al., 2010; C- Carboniferous: Algeo and Woods, 1994; Milana and Lopez, 1998; P- Permian: Ernesto and Pacca, 1981; J- Jurassic: Anderson and Kirkland, 1960; Anderson and Koopmans, 1963; Park and Fürsich, 2001; K- Cretaceous: Davies et al., 2012; Tian et al., 2021; Ma et al., 2021; E- Paleogene: Ripepe et al., 1991; Shunk et al., 2008; Shi et al., 2021; Q + N- Quaternary and Neogene: Cooper et al., 2000; Vonrad et al., 2002; Yin et al., 2007; Galloway et al., 2013.

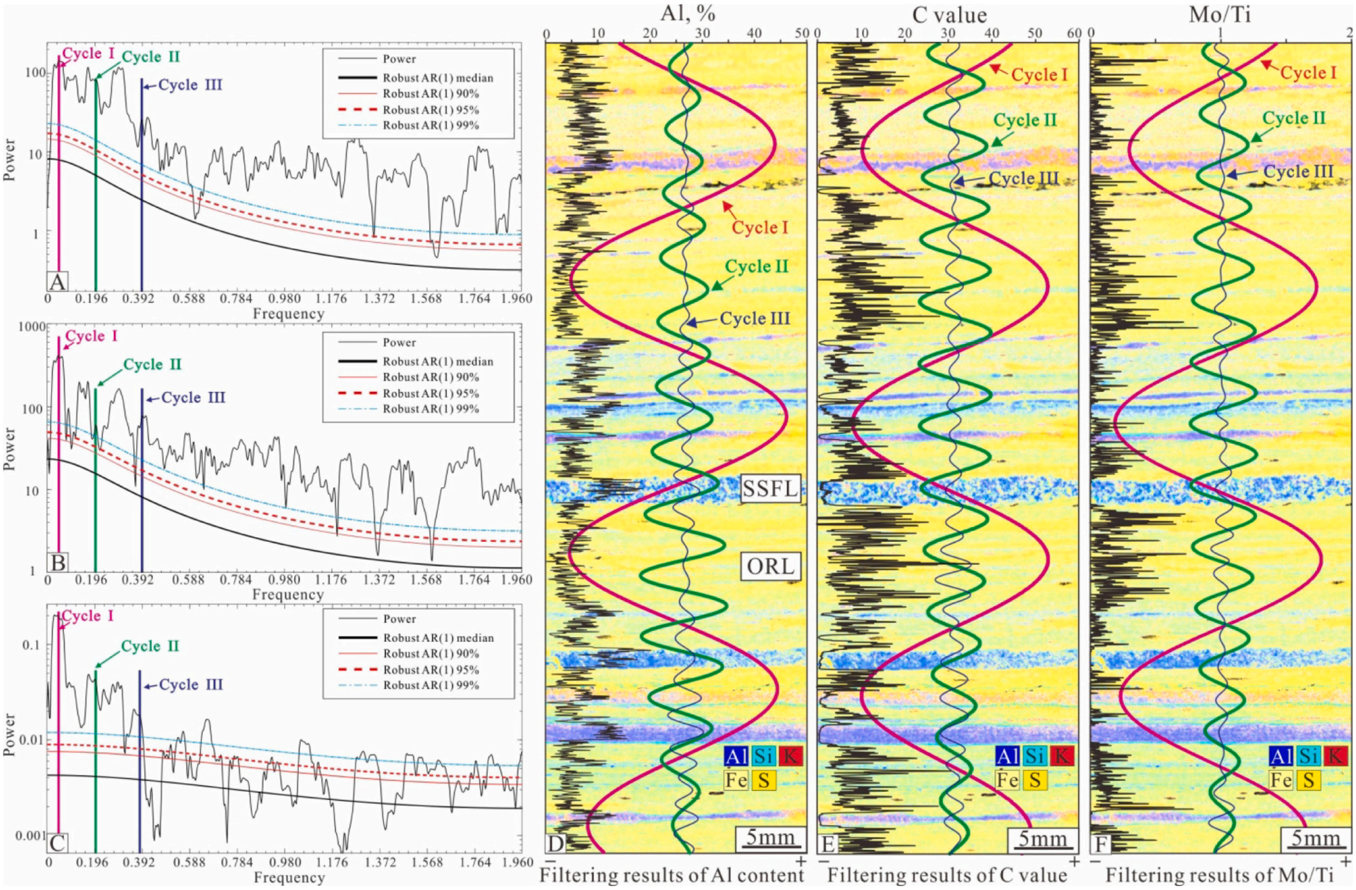

Fig. 9. Characteristics of paleo-environment evolution controlled by solar activity during the late Triassic. A, Spectral analysis of Al content. B, spectral analysis of C value. C, spectral analysis of Mo/Ti ratio. D, filtering results of Al content on cycle I (Gaussian filter, passband: 0.044 ± 0.004 cycles/mm), cycle II (Gaussian filter, passband: 0.198 ± 0.020 cycles/mm) and cycle III (Gaussian filter, passband: 0.386 ± 0.078 cycles/mm). E, filtering results of C value on cycle I (Gaussian filter, passband: 0.044 ± 0.004 cycles/mm), cycle II (Gaussian filter, passband: 0.201 ± 0.020 cycles/mm) and cycle III (Gaussian filter, passband: 0.378 ± 0.078 cycles/mm). F, filtering results of Mo/Ti ratio on cycle I (Gaussian filter, passband: 0.044 ± 0.004 cycles/mm), cycle II (Gaussian filter, passband: 0.197 ± 0.020 cycles/mm) and cycle III (Gaussian filter, passband: 0.380 ± 0.078 cycles/mm). The data of Al content, C value and Mo/Ti ratio in A-F are all obtained from the same shale samples, Well N70, 1714.96 m. SSFL- silt-sized felsic lamina, ORL- organic-rich lamina.

and the lake level during the period of intense solar activity (Qiu et al., 2015; Tombo et al., 2015). In contrast, when the C value and Mo/Ti ratio synchronously increase, Al content decreases, and silt-grained sediments gradually disappear (Fig. 9). This suggests that weak solar activity induced the increased humidity and lake-level rise in the Triassic (Qiu et al., 2015; Tombo et al., 2015).

In the interannual scale, the C value and Mo/Ti ratio changed in the 2–8 yr periodicity (Appendix A; Fig. 10A-C). In particular, the high Mo/Ti ratio and C value mainly correspond to the organic matter layer (Fig. 10B-C), while the low Mo/Ti ratio and C value mainly correspond to the clay mineral layer (Fig. 10B-C), which indicates that the time-scales of high frequency paleoenvironmental evolution is very similar to the timescales of cyclicities of Al contents on the micron scale (Fig. 7). Therefore, the short-term paleo-environmental oscillations controlled by the ENSO-like cycles were also worthy of attention during the late Triassic. The in-phase variation of the C value and Mo/Ti ratio in the 2–8 yr cycle is relatively obvious after cross-wavelet and wavelet coherence analyses (Figs. 10F, G). Intense water reducibility occurs during periods of high humidity, and vice versa (Figs. 10B, C). In the context of modern sea–land distribution, taking the Pacific Ocean as an example, the trade wind near the equator blew warm sea water towards the western Pacific during the non-ENSO period, inducing warm and cold pools in the western and eastern Pacific, respectively (Camargo and Sobel, 2005). During this period, the western Pacific coastal area (WPCA) experienced abundant rainfall, whereas the eastern Pacific coastal area (EPCA) remained relatively arid. During the ENSO period, the Pacific warm pool moved eastward, resulting in reduced and increased rainfall in the WPCA and EPCA, respectively (Camargo and Sobel, 2005). Therefore, the periodic movement of the warm pool controlled by ENSO eventually induced periodic variations of humidity in the WPCA. In the Triassic, the Ordos Basin was located in the coastal area of western Panthalassa (Scotese, 2014). The sea–land distribution at the Permian–Triassic boundary formed the warm and cold pools on both sides of the Panthalassa after paleoclimatic simulation (Shields and Kiehl, 2018). Western Panthalassa received more rainfall (warm pool) than eastern Panthalassa (cold pool) (Shields and Kiehl, 2018). The sea–land distribution in the Triassic and Permian–Triassic boundary are quite similar (Scotese, 2014). Therefore, we speculated that warm and cold pools also existed in the Triassic. This created significant conditions for the ENSO during the Triassic. Additionally, the greenhouse effect promoted the occurrence of ENSO (Davies et al., 2012). Robust ENSO signals have been confirmed in the past "greenhouse" episodes during late Cretaceous (Davies et al., 2012). In the Triassic "hot-house" world, therefore, the periodic evolution of humidity in the 2–8 yr period identified in the Ordos Basin is likely to relate to the ENSO occurring in the Triassic. Further identification of storm intensity and flood frequency in the coastal areas of western Panthalassa may be helpful in demonstrating the occurrence of the ENSO in the Triassic (Rodbell et al., 1999; Fuller et al., 2019).

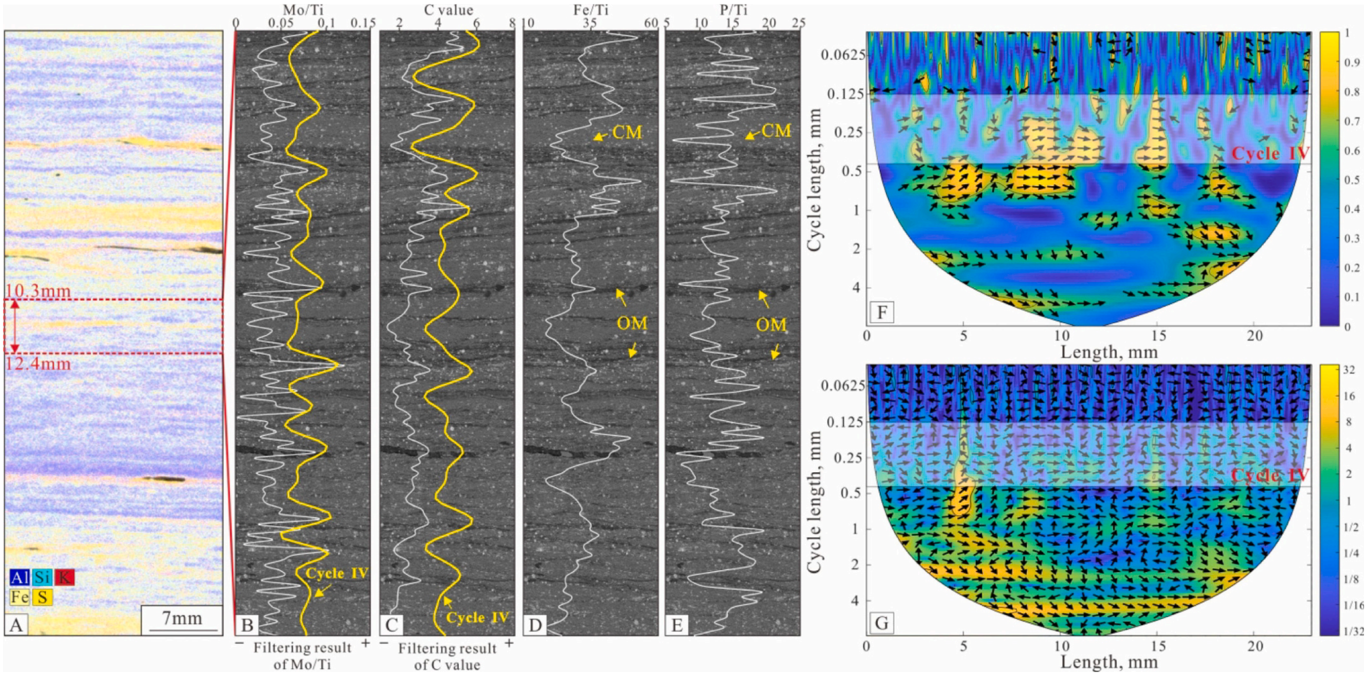

Fig. 10. Characteristics of paleo-environment evolution controlled by ENSO-like cycle during late Triassic. A, distribution of major elements of shale samples from Well Ch96, 2055.55 m. B, distribution and filtering result of Mo/Ti ratio (Gaussian filter, passband: 5.242 ± 2.808 cycles/mm). C, distribution and filtering result of C value (Gaussian filter, passband: 5.242 ± 2.808 cycles/mm). D, distribution of Fe/Ti ratio. E, distribution of P/Ti ratio; F, cross wavelet analysis of C value and Mo/Ti ratio. G, wavelet coherence analysis of C value and Mo/Ti ratio. OM-organic matter layer; CM-clay mineral layer.

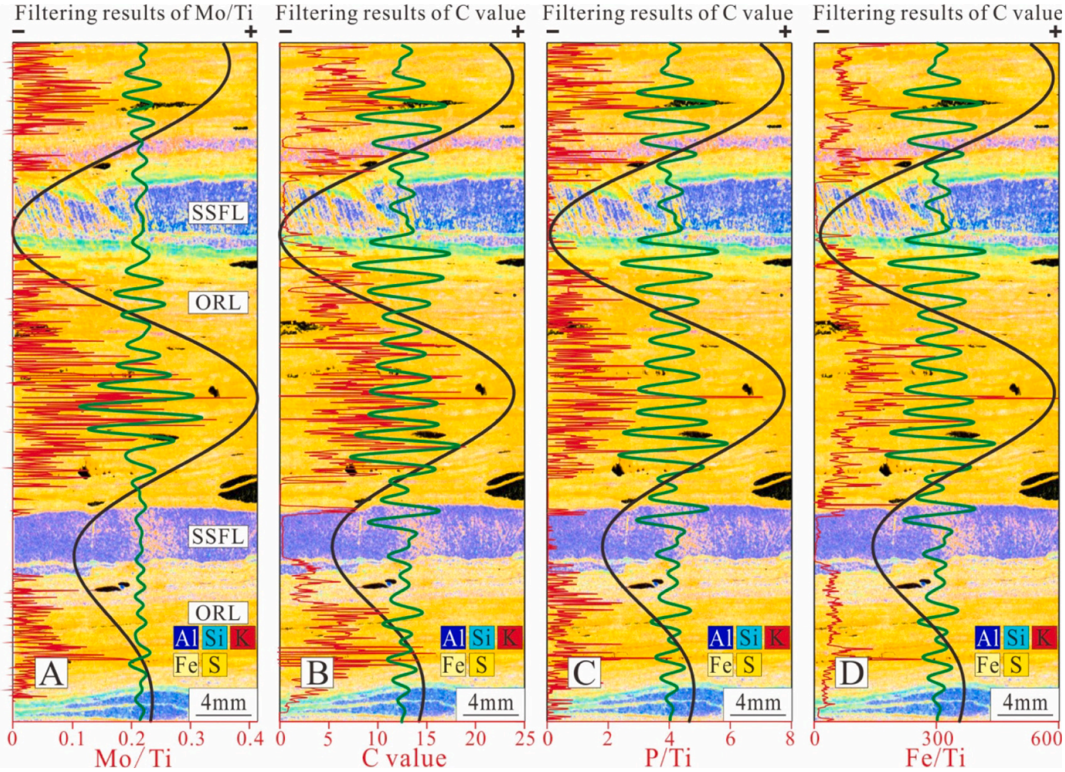

Fig. 11. Distribution of Mo/Ti, C value, P/Ti, Fe/Ti and their correspondence to the filtering results of Mo/Ti and C value. A, Distribution of Mo/Ti ratios and their filtering results of cycle I (Gaussian filter, passband: 0.037 ± 0.003 cycles/mm) and cycle III (Gaussian filter, passband: 0.675 ± 0.162 cycles/mm). B, distribution of C value and their filtering results of cycle I (Gaussian filter, passband: 0.037 ± 0.003 cycles/mm) and cycle III (Gaussian filter, passband: 0.637 ± 0.162 cycles/mm). C, distribution of P/Ti ratios and their correspondence to the filtering results of C value. D, distribution of Fe/Ti ratios and their correspondence to the filtering results of C value. The data of Mo/Ti, C value, P/Ti and Fe/Ti are all obtained from the same shale samples, Well N70, 1719.07 m. Micro-XRF analysis results, Mo/Ti and C values (including their filtering results) are referred from Lin et al. (2022). SSFL- silt-sized felsic lamina, ORL- organic-rich lamina.

5.3. *Implication of high-frequency paleo-environmental evolution for algal bloom*

Triassic paleo-environmental evolution was actually unstable, especially on short timescales, and high-frequency paleo-environmental fluctuations steadily occurred. Whether solar activity and ENSO-like cycles caused periodic evolution of the global ocean and lake environment remains to be verified in other locations worldwide. We also noticed that high-frequency paleo-environmental fluctuations are conducive to algal blooms. Solar activity and ENSO-like cycles induce a rapid increase in rainfall over a short period (Figs. 9E, 10C). The increased runoff caused by the intense rainfall promotes the input of nutrients into the lake basin (Zaw and Chiswell, 1999; James et al., 2008; Reichwaldt and Ghadouani, 2012), which is supported by the synchronous increase in the Fe/Ti and P/Ti ratios (Figs. 10D-E, 11). Massive inputs of nutrients (e.g. P, Fe), then, was beneficial to stimulate the algae blooms (Carrillo and Díaz-Villanueva, 2021).

Red algae occurring in lentoid and red color can be commonly identified in the shales from Chang 7_3 sub-member (Fig. 12A, B) (Kong, 2007). Energy spectrum analysis shows that the elements of calcium (Ca) and phosphorus (P) are enriched in the red algae fossils (Fig. 12C, D). According to the shale composition (Fig. 2C-E), however, the inorganic minerals in shales mainly enrich the elements of potassium (K), aluminum (Al), silicon (Si), sodium (Na), iron (Fe) and sulfur (S). This makes it possible to identify the spatial distribution of red algae using the element-enrichment features. After the surface scanning of element content using micro-XRF, we stack the element distribution maps of Ca and P, then identify the spatial distribution characteristics of red algae (Fig. 12E). The red algae distributes parallel to each other and mainly in the form of enrichment zone (Fig. 12E). The enrichment zones of red algae appear cyclically on the micron-scale, suggesting that the blooms of red algae may be controlled by high frequency paleoenvironmental oscillation. During the weak solar activity period in the 360–500 yr cycle I, increased rainfall, along with the influx of nutrients, promoted the proliferation of red algae (Fig. 12). In this context, high-frequency nutrient inputs controlled by the 30–57 yr cycle III further induced the red algae to enrich at intervals of decades (Fig. 12). In the semi-cycle of increased rainfall controlled by the ENSO-like cycle, organic layers were widely deposited (Figs. 10D, E). These organic layers in shale are believed to be products of algal blooms (Yang and Zhang, 2005). Frequent nutrient inputs controlled by solar activity and ENSO-like cycles create good conditions for algal blooms.

After the End-Permian mass extinction, the subsequent ecosystem recovery gradually resulted in a return to pre-extinction taxonomic diversity in the early Triassic (Sahney and Benton, 2008). The Carnian Pluvial Event during the late Triassic also caused partial extinction of marine and land life, followed by biotic recovery (Furin et al., 2006; Corso et al., 2018, 2020). The factors affecting biotic recovery received a lot of attention from researchers (Hermann et al., 2011; Chen and Benton, 2012; Feng et al., 2017; Luo et al., 2020). Microbial mats generally act as oxic oases with sufficient food resources, aiding the recovery of trace makers or eumetazoan animals after mass extinction (Brocks et al., 2017; Luo et al., 2020). Therefore, algal bloom is likely to play an important role in the promotion of biotic recovery.

After mass extinction, some researchers have argued that the injection of bio-available iron and zinc into the water column from volcanism promoted algal blooms (Chen et al., 2005; Xie et al., 2010; Jia et al., 2012; Saito et al., 2022). Others believe that volcanism-induced anoxic environment in the aftermath of mass extinction promoted the enrichment of ammonium, thereby inducing algal blooms (Sun et al., 2019). During the late Triassic, solar activity and ENSO-like cycles stably existed regardless of the periods of maximum or minimum obliquity (Appendix A). Continuous and high-frequency nutrient inputs controlled by these small-scale cycles directly induced algal blooms. Based on the deposition time of thick-bedded shales in the Chang 7_3 sub-member, frequent algal blooms exactly occurred in the CPE interval (Corso et al., 2020; Lu et al., 2021). Therefore, the facilitation of high-frequency paleo-environment evolution on algal blooms may also need to be considered in the research of biotic recovery during the CPE interval in the late Triassic.

6. Conclusion

This study confirms that the Triassic paleo-environmental evolution was actually unstable. In addition to the paleo-environmental disturbances induced by geological events, periodic paleo-environmental evolution existed in the Triassic. Based on the cyclical sedimentary records in the Triassic lacustrine sediments, it is recognized that: (1) astronomical cycles controlled the periodic evolution of paleo-environment on the millennium scale; (2) solar activity cycles,

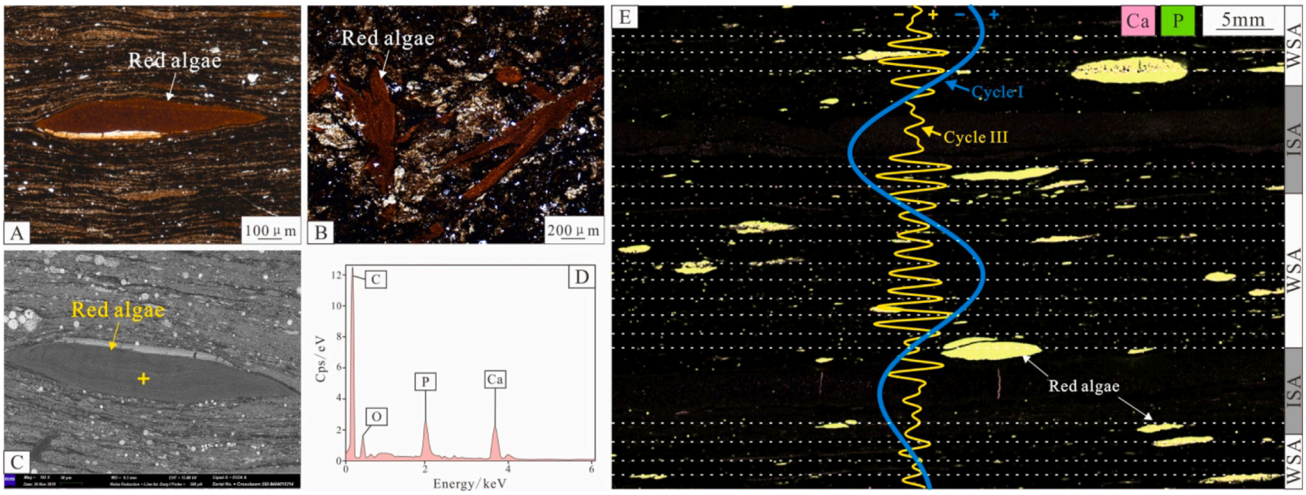

Fig. 12. The relationship between solar activity and algae bloom. A, Microscopic characteristics of red algae in the slice which is perpendicular to the lamina; B, microscopic characteristics of red algae in the slice which is parallel to the lamina; C, microscopic characteristics of red algae under SEM analysis; D, electron energy spectrum of the red algae obtained from the position of yellow cross in image C. E, distribution of red algae rich in the elements of calcium and phosphorus under micro-XRF analysis and their correspondence to the filtering results of C value (cycle I-passband: 0.037 ± 0.003 cycles/mm; cycle III- passband: 0.637 ± 0.162 cycles/mm). The lower the content of selected elements in the image E, the blacker it is. The white dotted lines in the image E indicate the enrichment zone of red algae. WSA- weak solar activity; ISA- intense solar activity. (For interpretation of the references to colour in this figure legend, the reader is referred to the web version of this article.) (For interpretation of the references to colour in this figure legend, the reader is referred to the web version of this article.)

including 360–500 yr cycle (cycle I), 81–110 yr cycle (cycle II), and 30–57 yr cycle (cycle III), impacted Triassic paleo-environmental evolution on the decadal–centennial scale; (3) the ENSO-like cycle (2–8 yr) induced high-frequency paleo-environmental evolution on the interannual scale.

Obliquity variations mainly induced changes in temperature, humidity, and water depth during the Triassic. In the mid-latitudes of the Northern Hemisphere, the increase in obliquity caused the temperature and humidity to rise, followed by an increase in the levels of lakes, and vice versa. The variations in eccentricity regulated the magnitude of obliquity-forced paleo-environmental evolution. With the background of paleo-environmental evolution caused by astronomical cycles, solar activity further induced cyclic fluctuations of humidity and lake-level. Intense solar activity resulted in humidity reduction and lake-level falling, whereas high humidity and high lake level appeared during periods of weak solar activity. The ENSO-like cycle also induced high-frequency oscillations of humidity and reducibility on a 2–8 yr scale. This suggests that the ENSO may have occurred during the Triassic.

High-frequency paleo-environmental evolution caused by solar activity and ENSO-like cycles further induced massive quantities of nutrients entering lakes within a brief period, which stimulated algal blooms. Red algae blooms occurred during a weak solar activity period in the 360–500 yr cycle I. In this context, the 30–57 yr cycle III further induced red algae enrichment at intervals of decades. ENSO-like cycles also promoted algal blooms and organic layer formation on a 2–8 yr scale.

Declaration of Competing Interest

The authors declare that they have no known competing financial interests or personal relationships that could have appeared to influence the work reported in this paper.

Data availability

Data will be made available on request.

Acknowledgement

This study was co-supported by the National Natural Science Foundation of China (Grant No. 42072161) and Innovation Research Group of the Natural Fund Committee (Grant No. 41821002) and Fundamental Research Funds for the Central Universities (Grant No. 22CX07008A). We would like to thank the Changqing Oilfield Company of PetroChina for providing the related core samples and geological data in Chang 7_3 sub-member, Ordos Basin.

Appendix A. Appendix

Cyclicality of Al content on thickness and timescales in lacustrine shales from Well N70 and Well Ch96. Cycle I-IV was obtained by spectrum analysis and wavelet analysis. The timescales of cycle I-IV present in this article correspond to the timescales in this Table. Timescale 1 indicates the timescale of thickness cycle (cycle I-IV) obtained by spectral analysis of Al; Timescale 2 indicates the timescale of thickness cycle (cycle I-IV) obtained by spectral analysis of Mo/Ti ratio; Timescale 3 indicates the timescale of thickness cycle (cycle I-IV) obtained by spectral analysis of C value. #-the shale deposited during the period of low obliquity; *-the shale deposited during the period of high obliquity. The Cycle I-III obtained by spectrum analysis and wavelet analysis of Mo/Ti ratio and C value in well N70 were refer to our another article (Lin et al., 2022). In this article, we combined two wells (N70 and Ch96) and three parameters (Al content, Mo/Ti ratio and C value) to further determine that the solar activity cycles were stably recorded in the thickly-bedded shales from Chang7_3 sub-member in the Ordos Basin.

Well	Depth, m	Cycle I/mm	Cycle II/mm	Cycle III/mm	Cycle IV/mm	Notes
N70	1713.58*	22.66	4.53	1.64	0.17–0.45	Al
		22.66	4.50	1.66	0.17–0.46	Mo/Ti
		22.66	4.43	1.64	0.17–0.45	C value
N70	1714.08*	19.03	4.64	1.94	0.11–0.36	Al
		19.03	4.64	1.90	0.12–0.36	Mo/Ti
		19.03	4.64	1.90	0.11–0.36	C value
N70	1714.42#	16.85	5.44	2.76	0.14–0.40	Al
		17.96	5.34	2.84	0.14–0.39	Mo/Ti
		17.96	5.62	2.84	0.14–0.40	C value
N70	1714.96#	22.55	5.05	2.59	0.15–0.32	Al
		22.55	5.07	2.63	0.15–0.35	Mo/Ti
		22.55	4.97	2.64	0.15–0.32	C value
N70	1718.3#	18.38	4.26	2.73	0.19–0.41	Al
		18.21	4.26	2.71	0.18–0.41	Mo/Ti
		18.21	4.26	2.73	0.19–0.43	C value
N70	1718.9*	24.29	4.07	1.87	0.13–0.36	Al
		24.29	4.05	1.87	0.13–0.34	Mo/Ti
		24.29	4.05	1.87	0.13–0.36	C value
N70	1719.2*	27.68	5.93	1.87	0.11–0.35	Al
		26.56	5.91	1.83	0.10–0.39	Mo/Ti
		26.56	5.91	1.87	0.11–0.36	C value
N70	1719.07*	26.68	/	1.48	0.11–0.38	Al
		26.68	/	1.48	0.11–0.38	Mo/Ti
		26.68	/	1.57	0.11–0.38	C value
N70	1720.7#	24.48	5.19	2.28	0.11–0.32	Al
		24.48	5.19	2.28	0.11–0.32	Mo/Ti
		24.48	5.19	2.28	0.11–0.32	C value
Ch96	2054.9#	/	5.45	2.24	0.15–0.39	Al
		/	5.21	2.24	0.15–0.37	Mo/Ti
		/	5.45	2.24	0.15–0.39	C value
Ch96	2055.55#	/	4.42	2.45	0.13–0.38	Al

(continued on next page)

(*continued*)

Well	Depth, m	Cycle I/mm	Cycle II/mm	Cycle III/mm	Cycle IV/mm	Notes
		/	4.42	2.45	0.13–0.38	Mo/Ti
		/	4.42	2.45	0.13–0.38	C value
Ch96	2057$^{\#}$	/	5.05	2.63	0.12–0.18	Al
		/	5.05	2.63	0.16–0.19	Mo/Ti
		/	5.05	2.63	0.13–0.19	C value
Ch96	2065.8*	/	6.02	1.62	0.11–0.40	Al
		/	6.02	1.57	0.11–0.40	Mo/Ti
		/	6.02	1.57	0.12–0.40	C value
Ch96	2068.8$^{\#}$	/	/	3.17	0.11–0.38	Al
		/	/	3.17	0.11–0.39	Mo/Ti
		/	/	3.17	0.12–0.38	C value
Ch96	2070.05*	/	5.38	2.83	0.11–0.38	Al
		/	5.38	2.83	0.10–0.40	Mo/Ti
		/	5.38	2.83	0.10–0.40	C value
Timescales 1		**360–500 yr**	**81–110 yr**	**30–57 yr**	**2.0–8.0 yr**	Al
Timescales 2		**360–500 yr**	**81–110 yr**	**30–57 yr**	**2.0–8.0 yr**	Mo/Ti
Timescales 3		**360–500 yr**	**81–110 yr**	**30–57 yr**	**2.0–8.0 yr**	C value

Appendix B. Supplementary data

Supplementary data to this article can be found online at https://doi.org/10.1016/j.palaeo.2022.111376.

References

Algeo, T.J., Woods, A.D., 1994. Microstratigraphy of the Lower Mississippian Sunbury Shale: A record of solar-modulated climatic cyclicity. Geology 22 (9), 795–798.

Anderson, R.Y., Dean, W.E., 1988. Lacustrine varve formation through time. Palaeogeogr. Palaeoclimatol. Palaeoecol. 62 (1–4), 215–235.

Anderson, R.Y., Kirkland, D.W., 1960. Origin, varves, and cycles of Jurassic Todilto formation, New Mexico. AAPG Bull. 44 (1), 37–52.

Anderson, R.Y., Koopmans, L.H., 1963. Harmonic analysis of varve time series. J. Geophys. Res. 68 (3), 877–893.

Andrews, S.D., Trewin, N.H., Hartley, A.J., Weedon, G.P., 2010. Solar variance recorded in lacustrine deposits from the Devonian and Proterozoic of Scotland. J. Geol. Soc. Lond. 167, 847–856.

Bal, S., Bose, M., 2010. A climatological study of the relations among solar activity, galactic cosmic ray and precipitation on various regions over the globe. J. Earth Syst. Sci. 119 (2), 201–209.

Baldwin, M.P., Gray, L.J., Dunkerton, T.J., Hamilton, K., Haynes, P.H., Randel, W.J., Holton, J.R., Alexander, M.J., Hirota, I., Horinouchi, T., Jones, D.B.A., Kinnersley, J. S., Marquardt, C., Sato, K., Takahashi, M., 2001. The quasi-biennial oscillation. Rev. Geophys. 39 (2), 179–229.

Berger, A., Loutre, M.F., Dehant, V., 1989. Pre-quaternary Milankovitch frequencies. Nature (London) 342, 6246.

Bourget, J., Zaragosi, S., Ellouz-Zimmermann, S., Ducassou, E., Prins, M.A., Garlan, T., Lanfumey, V., Schneider, J.L., Rouillard, P., Giraudeau, J., 2010. Highstand vs. lowstand turbidite system growth in the Makran active margin: Imprints of high-frequency external controls on sediment delivery mechanisms to deep water systems. Mar. Geol. 274, 187–208.

Brocks, J.J., Jarrett, A.J., Sirantoine, E., Hallmann, C., Hoshino, Y., Liyanage, T., 2017. The rise of algae in Cryogenian oceans and the emergence of animals. Nature 548 (7669), 578–581.

Brucker, R.P., McManus, J., Severmann, S., Owens, J., Lyons, T.W., 2011. Trace metal enrichments in Lake Tanganyika sediments: Controls on trace metal burial in lacustrine systems. Geochim. Cosmochim. Acta 75 (2), 483–499.

Camargo, S.J., Sobel, A.H., 2005. Western North Pacific tropical cyclone intensity and ENSO. J. Clim. 18 (15), 2996–3006.

Carrillo, U., Díaz-Villanueva, V., 2021. Impacts of volcanic eruptions and early recovery in freshwater environments and organisms. Biol. Rev. 96 (6), 2546–2560.

Carroll, A.R., Graham, S.A., Smith, M.E., 2010. Walled sedimentary basins of China. Basin Res. 22 (1), 17–32.

Carslaw, K.S., Harrison, R.G., Kirkby, J., 2002. Cosmic rays, clouds, and climate. Science 198 (5599), 1732–1737.

Chen, Z.Q., Benton, M.J., 2012. The timing and pattern of biotic recovery following the end-Permian mass extinction. Nat. Geosci. 5 (6), 375–383.

Chen, D., Qing, H., Li, R., 2005. The Late Devonian Frasnian–Famennian (F/F) biotic crisis: insights from $\delta^{13}C_{carb}$, $\delta^{13}C_{org}$ and $^{87}Sr/^{86}Sr$ isotopic systematics. Earth Planet. Sci. Lett. 235 (1–2), 151–166.

Clausing, A., Boy, J.A., 2000. Lamination and primary production in fossil lakes: relationship to paleoclimate in the Carboniferous- Permian transition. Geol. Soc. Lond. Spec. Publ. 181 (1), 5–16.

Clemmensen, L.B., Kent, D.V., Jenkins Jr., F.A., 1998. A Late Triassic lake system in East Greenland: facies, depositional cycles and palaeoclimate. Palaeogeogr. Palaeoclimatol. Palaeoecol. 140 (1–4), 135–159.

Cooper, M.C., O'Sullivana, P.E., Shineb, A.J., 2000. Climate and solar variability recorded in Holocene laminated sediments-a preliminary assessment. Quat. Int. 68-71, 363–371.

Corso, D.J., Mietto, P., Newton, R.J., Pancost, R.D., Preto, N., Roghi, G., Wignall, P.B., 2012. Discovery of a major negative $\delta^{13}C$ spike in the Carnian (Late Triassic) linked to the eruption of Wrangellia flood basalts. Geology 40 (1), 79–82.

Corso, D.J., Ruffell, A., Preto, N., 2018. The Carnian pluvial episode (Late Triassic): new insights into this important time of global environmental and biological change. J. Geol. Soc. 175 (6), 986–988.

Corso, D.J., Bernardi, M., Sun, Y., Song, H., Seyfullah, L.J., Preto, N., Gianolla, P., Ruffell, A., Kustatscher, E., Roghi, G., Merico, A., Hohn, S., Shmidt, A.R., Marzoli, A., Newton, R., Wignall, P.B., Benton, M.J., 2020. Extinction and dawn of the modern world in the Carnian (Late Triassic). Science. Advances 6 (38), eaba0099.

Damon, P.E., Sonnett, C.P., 1991. Solar and terrestrial components of the atmospheric 14C variation spectrum. In: Sonnett, C.P., Giampapa, M.S., Matthews, M.S. (Eds.), The Sun in Time. The University of Arizona Press, Tucson, Ariz, pp. 360–388.

Davies, A., Kemp, A.E., Weedon, G.P., Barron, J.A., 2012. El Niño-southern oscillation variability from the late cretaceous Marca shale of California. Geology 40 (1), 15–18.

De Boer, B., Lourens, L.J., Van De Wal, R.S., 2014. Persistent 400,000-year variability of Antarctic ice volume and the carbon cycle is revealed throughout the Plio-Pleistocene. Nat. Commun. 5 (1), 1–8.

Dean, J.M., Kemp, A.E., 2004. A 2100 year BP record of the Pacific decadal oscillation, El Niño Southern Oscillation and quasi-biennial oscillation in marine production and fluvial input from Saanich Inlet, British Columbia. Palaeogeogr. Palaeoclimatol. Palaeoecol. 213 (3–4), 207–229.

Dicke, R.H., 1979. Solar luminosity and the sunspot cycle. Nature 280 (5717), 24–27.

Du, X., Hendy, I., Hinnov, L., Brown, E., Zhu, J., Poulsen, C.J., 2021. High-resolution interannual precipitation reconstruction of Southern California: Implications for Holocene ENSO evolution. Earth Planet. Sci. Lett. 554, 116670.

Ernesto, M., Pacca, I.G., 1981. Spectral analysis of Permocarboniferous geomagnetic variation data from glacial rhythmites. Geophys. J. Int. 67 (3), 641–647.

Fagel, N., Boës, X., Loutre, M.F., 2008. Climate oscillations evidenced by spectral analysis of Southern Chilean lacustrine sediments: the assessment of ENSO over the last 600 years. J. Paleolimnol. 39 (2), 253–266.

Feng, X., Chen, Z.Q., Woods, A., Fang, Y., 2017. A Smithian (Early Triassic) ichnoassemblage from Lichuan, Hubei Province, South China: Implications for biotic recovery after the latest Permian mass extinction. Palaeogeogr. Palaeoclimatol. Palaeoecol. 486, 123–141.

Foster, W.J., Sebe, K., 2017. Recovery and diversification of marine communities following the late Permian mass extinction event in the western Palaeotethys. Glob. Planet. Chang. 155, 165–177.

Fu, J.H., Li, S.X., Xu, L.M., Niu, X.B., 2018. Paleo-sedimentary environmental restoration and its significance of Chang 7 Member of Triassic Yanchang Formation in Ordos Basin, NW China. Pet. Explor. Dev. 45 (6), 998–1008.

Fu, J.H., Li, S.X., Niu, X.B., Deng, X.Q., Zhou, X.P., 2020. Geological characteristics and exploration of shale oil in Chang 7 Member of Triassic Yanchang Formation, Ordos Basin, NW China. Pet. Explor. Dev. 47 (5), 931–945.

Fuller, I.C., Macklin, M.G., Toonen, W.H., Turner, J., Norton, K., 2019. A 2000 year record of palaeofloods in a volcanically-reset catchment: Whanganui River, New Zealand. Glob. Planet. Chang. 181, 102981.

Furin, S., Preto, N., Rigo, M., Roghi, G., Gianolla, P., Crowley, J.L., Bowring, S.A., 2006. High-precision U-Pb zircon age from the Triassic of Italy: Implications for the Triassic time scale and the Carnian origin of calcareous nannoplankton and dinosaurs. Geology 34 (12), 1009–1012.

Galfetti, T., Bucher, H., Martini, R., Hochuli, P.A., Weissert, H., Crasquin-Soleau, S., Brayard, A., Goudemand, N., Brühwiler, T., Guodun, K., 2008. Evolution of Early Triassic outer platform paleoenvironments in the Nanpanjiang Basin (South China) and their significance for the biotic recovery. Sediment. Geol. 204 (1–2), 36–60.

Galloway, J.M., Wigston, A., Patterson, R.T., Swindles, G.T., Reinhardt, E., Roe, H.M., 2013. Climate change and decadal to centennial-scale periodicities recorded in a late Holocene NE Pacific marine record: Examining the role of solar forcing. Palaeogeogr. Palaeoclimatol. Palaeoecol. 386, 669–689.

Grasby, S.E., Shen, W., Yin, R., Gleason, J.D., Blum, J.D., Lepak, R.F., Hurley, J.P., Beauchamp, B., 2017. Isotopic signatures of mercury contamination in latest Permian oceans. Geology 45 (1), 55–58.

Gray, L.J., Beer, J., Geller, M., Haigh, J.D., Lockwood, M., Matthes, K., Cubasch, U., Fleitmann, D., Harrison, G., Hood, L., Luterbacher, J., Meehl, G.A., Shindell, D., Van Geel, B., White, W., 2010. Solar influences on climate. Rev. Geophys. 48 (4), 1–53.

Hammer, Ø., Harper, D.A., Ryan, P.D., 2001. PAST: Paleontological statistics software package for education and data analysis. Palaeontol. Electron. 4 (1), 9.

Hayashi, K.I., Fujisawa, H., Holland, H.D., Ohmoto, H., 1997. Geochemistry of~ 1.9 Ga sedimentary rocks from northeastern Labrador, Canada. Geochim. Cosmochim. Acta 61 (19), 4115–4137.

Hermann, E., Hochuli, P.A., Méhay, S., Bucher, H., Brühwiler, T., Ware, D., Hautmann, M., Roohi, G., ur-Rehman, K., Yaseen, A., 2011. Organic matter and palaeoenvironmental signals during the Early Triassic biotic recovery: The Salt Range and Surghar Range records. Sediment. Geol. 234 (1–4), 19–41.

Hinnov, L.A., Goldhammer, R.K., 1991. Spectral analysis of the Middle Triassic Latemar limestone. J. Sediment. Res. 61 (7), 1173–1193.

Hornung, J., Aigner, T., 1999. Reservoir and aquifer characterization of fluvial architectural elements: Stubensandstein, Upper Triassic, southwest Germany. Sediment. Geol. 129 (3–4), 215–280.

Hoyt, D.V., Schatten, K.H., 1998. Group sunspot numbers: a new solar activity reconstruction. Sol. Phys. 179, 189–219.

Huang, H., Gao, Y., Ma, C., Jones, M.M., Zeeden, C., Ibarra, D.E., Wu, H.C., Wang, C.S., 2021. Organic carbon burial is paced by a~ 173-ka obliquity cycle in the middle to high latitudes. Science. Advances 7 (28), eabf9489.

James, R.T., Chimney, M.J., Sharfstein, B., Engstrom, D.R., Schottler, S.P., East, T., Jin, K.R., 2008. Hurricane effects on a shallow lake ecosystem, Lake Okeechobee, Florida (USA). Fundam. Appl. Limnol. 172 (4), 273–287.

Jia, C., Huang, J., Kershaw, S., Luo, G., Farabegoli, E., Perri, M.C., Chen, L., Bai, X., Xie, S., 2012. Microbial response to limited nutrients in shallow water immediately after the end-Permian mass extinction. Geobiology 10 (1), 60–71.

Kane, R.P., 2006. Spectral characteristics of Atlantic seasonal storm frequency. Mausam 57 (4), 597–608.

Kiessling, W., 2010. Reef expansion during the Triassic: Spread of photosymbiosis balancing climatic cooling. Palaeogeogr. Palaeoclimatol. Palaeoecol. 290 (1–4), 11–19.

Kong, Q.F., 2007. The organic maceral characteristics of Yanchang source rock in Ordos Basin. Xinjiang Petrol. Geol. 28 (2), 163–166.

Kong, X., Wang, Y., Wu, J., Cheng, H., 2003. A continuous 3000-year precipitation record of ENSO variability during LGM from a stalagmite in Nanjing. Chin. Sci. Bull. 48 (5), 480–484.

Kuiper, K.F., Deino, A., Hilgen, F.J., Krijgsman, W., Renne, P.R., Wijbrans, A.J., 2008. Synchronizing rock clocks of Earth history. Science 320 (5875), 500–504.

Li, K.J., Su, T.W., Liang, H.F., 2004. Cycle of sunspot activity based on modern observation. Chin. Sci. Bull. 49, 2511–2516.

Li, M., Huang, C., Hinnov, L., Ogg, J., Chen, Z.Q., Zhang, Y., 2016. Obliquity-forced climate during the Early Triassic hothouse in China. Geology 44 (8), 623–626.

Li, P., Tang, D., Shi, X., Jiang, G., Zhao, X., Zhou, X., Wang, X., Chen, X., 2018a. Sunspot cycles recorded in siliciclastic biolaminites at the dawn of the Neoproterozoic Sturtian glaciation in South China. Precambrian Res. 315, 75–91.

Li, M., Hinnov, L.A., Huang, C., Ogg, J.G., 2018b. Sedimentary noise and sea levels linked to land–ocean water exchange and obliquity forcing. Nat. Commun. 9 (1), 1–12.

Li, M., Hinnov, L.A., Kump, L., 2019. Acycle: time-series analysis software for paleoclimate research and education. Comput. Geosci. 127, 12–22.

Lin, M.R., Xi, K.L., Cao, Y.C., Zhu, R.K., Niu, X.B., Xin, H.G., Ma, W.J., 2022. Cyclicity related to solar activity in lacustrine organic-rich shales and their significance to shale-oil reservoir formation. Under Review.

Liu, Y., Huang, C., Ogg, J.G., Algeo, T.J., Kemp, D.B., Shen, W., 2019. Oscillations of global sea-level elevation during the Paleogene correspond to 1.2-Myr amplitude modulation of orbital obliquity cycles. Earth Planet. Sci. Lett. 522, 65–78.

Liu, D., Huang, C., Kemp, D.B., Li, M., Ogg, J.G., Yu, M., Foster, W.J., 2021a. Paleoclimate and sea level response to orbital forcing in the Middle Triassic of the eastern Tethys. Glob. Planet. Chang. 199, 103454.

Liu, X.Y., Li, S.X., Guo, Q.H., Zhou, X.P., Liu, J.Y., 2021b. Characteristics of rock types and exploration significance of the shale strata in the Chang 7_3 submember of Yanchang Formation, Ordos Basin. Nat. Gas Geosci. 32 (8), 1177–1189.

Lu, J., Zhang, P., Dal Corso, J., Yang, M., Wignall, P.B., Greene, S.E., Shao, L.Y., Lyu, D., Hilton, J., 2021. Volcanically driven lacustrine ecosystem changes during the Carnian Pluvial Episode (Late Triassic). Proc. Natl. Acad. Sci. 118 (40), e2109895118.

Lucio, P.S., 2005. Learning with solar activity influence on Portugal's rainfall: A stochastic overview. Geophys. Res. Lett. 32, L23819.

Lückge, A., Doose-Rolinski, H., Khan, A.A., Schulz, H., Rad, U.V., 2001. Monsoonal variability in the northeastern Arabian Sea during the past 5000 years: Geochemical evidence from laminated sediments. Palaeogeogr. Palaeoclimatol. Palaeoecol. 167 (3–4), 273–286.

Luo, M., Shi, G.R., Buatois, L.A., Chen, Z.Q., 2020. Trace fossils as proxy for biotic recovery after the end-Permian mass extinction: A critical review. Earth Sci. Rev. 203, 103059.

Ma, C., Hinnov, L.A., Eldrett, J.S., Meyers, S.R., Bergman, S.C., Minisini, D., Lutz, B., 2021. Centennial to millennial variability of greenhouse climate across the mid-Cenomanian event. Geology 50 (2), 227–231.

Magny, M., Arnaud, F., Holzhauser, H., Chapron, E., Debret, M., Desmet, M., Leroux, A., Millet, L., Revel, M., Vannière, B., 2010. Solar and proxy-sensitivity imprints on paleohydrological records for the last millennium in west-central Europe. Quat. Res. 73, 173–179.

Martindale, R.C., Foster, W.J., Velledits, F., 2019. The survival, recovery, and diversification of metazoan reef ecosystems following the end-Permian mass extinction event. Palaeogeogr. Palaeoclimatol. Palaeoecol. 513, 100–115.

Milana, J.P., Lopez, S., 1998. Solar cycles recorded in Carboniferous glacimarine rhythmites (Western Argentina): relationships between climate and sedimentary environment. Palaeogeogr. Palaeoclimatol. Palaeoecol. 144, 37–63.

Naeher, S., Gilli, A., North, R.P., Hamann, Y., Schubert, C.J., 2013. Tracing bottom water oxygenation with sedimentary Mn/Fe ratios in Lake Zurich, Switzerland. Chem. Geol. 352, 125–133.

Nambiar, R., Bhushan, R., Raj, H., 2022. Paleoredox conditions of bottom water in the northern Indian Ocean since 39 ka. Palaeogeogr. Palaeoclimatol. Palaeoecol. 586, 110766.

Park, M.H., Fürsich, F., 2001. Cyclic nature of lamination in the Tithonian Solnhofen Plattenkalk of southern Germany and its palaeoclimatic implications. Int. J. Earth Sci. 90, 847–854.

Parrish, J.T., 1993. Climate of the supercontinent Pangea. J. Geol. 101 (2), 215–233.

Peng, C., Zou, C., Zhang, S., Wu, H., Lü, Q., Hou, H., Wang, C., 2020. Astronomically forced variations in multiresolution resistivity logs of lower Upper Cretaceous (Cenomanian-Coniacian) terrestrial formations from the Songliao Basin, northeastern China. Palaeogeogr. Palaeoclimatol. Palaeoecol. 555, 109858.

Percival, L.M., Ruhl, M., Hesselbo, S.P., Jenkyns, H.C., Mather, T.A., Whiteside, J.H., 2017. Mercury evidence for pulsed volcanism during the end-Triassic mass extinction. Proc. Natl. Acad. Sci. 114 (30), 7929–7934.

Preto, N., Kustatscher, E., Wignall, P.B., 2010. Triassic climates-state of the art and perspectives. Palaeogeogr. Palaeoclimatol. Palaeoecol. 290 (1–4), 1–10.

Qiu, X.W., Liu, C.Y., Mao, G.Z., Deng, Y., Wang, F.F., Wang, J.Q., 2015. Major, trace and platinum-group element geochemistry of the Upper Triassic nonmarine hot shales in the Ordos basin, Central China. Appl. Geochem. 53, 42–52.

Raymo, M.E., Nisancioglu, K.H., 2003. The 41 kyr world: Milankovitch's other unsolved mystery. Paleoceanography 18 (1), 1–6.

Reichwaldt, E.S., Ghadouani, A., 2012. Effects of rainfall patterns on toxic cyanobacterial blooms Bin a changing climate: Between simplistic scenarios and complex dynamics. Water Res. 46 (5), 1372–1393.

Reinhardt, L., Ricken, W., 2000. The stratigraphic and geochemical record of Playa Cycles: monitoring a Pangaean monsoon-like system (Triassic, Middle Keuper, S. Germany). Palaeogeogr. Palaeoclimatol. Palaeoecol. 161 (1–2), 205–227.

Ripepe, M., Roberts, L.T., Fischer, A.G., 1991. ENSO and sunspot cycles in varved Eocene oil shales from image analysis. J. Sediment. Res. 61 (7), 1155–1163.

Rodbell, D.T., Seltzer, G.O., Anderson, D.M., Abbott, M.B., Enfield, D.B., Newman, J.H., 1999. An ~15000-year record of El Niño-driven alluviation in southwestern Ecuador. Science 283 (5401), 516–520.

Sageman, B.B., Rich, J., Arthur, M.A., Birchfield, G.E., Dean, W.E., 1997. Evidence for Milankovitch periodicities in Cenomanian-Turonian lithologic and geochemical cycles, Western Interior USA. J. Sediment. Res. 67 (2), 286–302.

Sahney, S., Benton, M.J., 2008. Recovery from the most profound mass extinction of all time. Proc. R. Soc. B Biol. Sci. 275 (1636), 759–765.

Saito, R., Tian, L., Kaiho, K., Takahashi, S., 2022. Biomarker evidence of prolongation of multiple phytoplankton blooms in the aftermath of the end-Permian mass extinction. Palaeogeogr. Palaeoclimatol. Palaeoecol. 111077.

Scotese, C.R., 2014. Atlas of Permo-Carboniferous Paleogeographic Maps (Mollweide Projection), Maps 53–64, Volumes 4. The Late Paleozoic, PALEOMAP Atlas for ArcGIS, PALEOMAP Project, Evanston, IL.

Shi, J.Y., Jin, Z.J., Liu, Q.Y., Fan, T.L., Gao, Z.Q., 2021. Sunspot cycles recorded in Eocene lacustrine fine-grained sedimentary rocks in the Bohai Bay Basin, eastern China. Glob. Planet. Chang. 205, 103614.

Shields, C.A., Kiehl, J.T., 2018. Monsoonal precipitation in the Paleo-Tethys warm pool during the latest Permian. Palaeogeogr. Palaeoclimatol. Palaeoecol. 491, 123–136.

Shunk, A.J., Driese, S.G., Dunbar, J.A., 2008. Late Tertiary paleoclimatic interpretation from lacustrine rhythmites in the Gray Fossil Site, northeastern Tennessee, USA. J. Paleolimnol. 42, 11–24.

Song, M., Zhou, A., Zhang, X., Zhao, C., He, Y., Yang, W., Liu, W., Li, S.H., Liu, Z., 2015. Solar imprints on Asian inland moisture fluctuations over the last millennium. The Holocene 25 (12), 1935–1943.

Sun, Y.D., Zulla, M.J., Joachimski, M.M., Bond, D.P.G., Wignall, P.B., Zhang, Z.T., Zhang, M.H., 2019. Ammonium ocean following the end-Permian mass extinction. Earth Planet. Sci. Lett. 518, 211–222.

Tang, D., Shi, X., Jiang, G., 2014. Sunspot cycles recorded in Mesoproterozoic carbonate biolaminites. Precambrian Res. 248, 1–16.

Tanner, L.H., Lucas, S.G., Chapman, M.G., 2004. Assessing the record and causes of Late Triassic extinctions. Earth Sci. Rev. 65 (1–2), 103–139.

Thibodeau, A.M., Ritterbush, K., Yager, J.A., West, A.J., Ibarra, Y., Bottjer, D.J., Berelson, W.M., Bergquist, B.A., Corsetti, F.A., 2016. Mercury anomalies and the timing of biotic recovery following the end-Triassic mass extinction. Nat. Commun. 7 (1), 1–8.

Tian, X., Gao, Y., Kukla, T., Lenz, O., Huang, H., Ibarra, D.E., Sun, S.L., Wang, C., 2021. Early Cretaceous solar cycles recorded in lacustrine laminations in North China. Am. J. Sci. 321 (9), 1285–1307.

Tombo, S.L., Dennielou, B., Berne, S., Bassetti, M.A., Toucanne, S., Jorry, S.J., Jouet, G., Fontanier, C., 2015. Sea-level control on turbidite activity in the Rhone canyon and the upper fan during the Last Glacial Maximum and Early deglacial. Sediment. Geol. 323, 148–166.

Trotter, J.A., Williams, I.S., Nicora, A., Mazza, M., Rigo, M., 2015. Long-term cycles of Triassic climate change: a new δ18O record from conodont apatite. Earth Planet. Sci. Lett. 415, 165–174.

Van Geel, B., Raspopov, O.M., Renssen, H., Van der Plicht, J., Dergachev, V.A., Meijer, H. A.J., 1999. The role of solar forcing upon climate change. Quat. Sci. Rev. 18 (3), 331–338.

Vonrad, U., Khan, A.A., Berger, W.H., Rammlmair, D., Treppke, U., 2002. Varves, turbidites and cycles in upper Holocene sediments (Makran slope, northern Arabian Sea). Geol. Soc. Lond., Spec. Publ. 195 (1), 387–406.

Wu, N., Rousseau, D.D., Liu, X., 2000. Response of mollusk assemblages from the Luochuan loess section to orbital forcing since the last 250 ka. Chin. Sci. Bull. 45 (17), 1617–1622.

Wu, H.C., Zhang, S.H., Feng, Q.L., Fang, N.Q., Yang, T.S., Li, H.Y., 2011. Theoretical basis, research advancement and prospects of cyclostratigraphy. Earth Sci. J. China Univ. Geosci. 36 (4), 409–427.

Xie, S., Pancost, R.D., Wang, Y., Yang, H., Wignall, P.B., Luo, G., Jia, C., Chen, L., 2010. Cyanobacterial blooms tied to volcanism during the 5 my Permo-Triassic biotic crisis. Geology 38 (5), 447–450.

Yang, H., Zhang, W.Z., 2005. Leading effect of the seventh Member high-quality source rock or Yanchang Formation in Ordos Basin during the enrichment of low-penetrating oil-gas accumulation: Geology and geochemistry. Geochimica 34 (2), 147–154.

Yin, Z.Q., Ma, L.H., Han, Y.B., Han, Y.G., 2007. Long-term variations of solar activity. Chin. Sci. Bull. 52 (20), 2737–2741.

Zaw, M., Chiswell, B., 1999. Iron and manganese dynamics in lake water. Water Res. 33 (8), 1900–1910.

Zhang, W.Z., Yang, H., Xia, X.Y., Xie, L.Q., Xie, G.W., 2016. Triassic chrysophyte cyst fossils discovered in the Ordos Basin, China. Geology 44 (12), 1031–1034.

Zhang, T., Li, Y., Fan, T., Da Silva, A.C., Shi, J., Gao, Q., Kuang, M.Z., Liu, W.W., Gao, Z. Q., Li, M.S., 2022. Orbitally-paced climate change in the early Cambrian and its implications for the history of the Solar System. Earth Planet. Sci. Lett. 583, 117420.

Zhao, X.H., Feng, X.S., 2015. Correlation between solar activity and the local temperature of Antarctica during the past 11,000 years. J. Atmos. Sol. Terr. Phys. 122, 26–33.

Zhao, W.Z., Zhu, R.K., Hu, S.Y., Hou, L.H., Wu, S.T., 2020. Accumulation contribution differences between lacustrine organic-rich shales and mudstones and their significance in shale oil evaluation. Pet. Explor. Dev. 47 (6), 1160–1171.

Zhou, D.W., Zhao, C.Y., Li, Y.D., Jian, W.C., Ye, J., Chen, G., 1995. Geological features of southwest margin of Ordos basin and its relationships with Qinling orogenic belt. Geological Publishing House, Beijing.